Journal of Petroleum Science and Engineering 155 (2017) 78–88

Contents lists available at ScienceDirect

Journal of Petroleum Science and Engineering

journal homepage: www.elsevier.com/locate/petrol

Experimental and simulation study of carbon dioxide, brine, and muscovite surface interactions

Craig M. Tenney[a,*], Thomas Dewers[a], Kuldeep Chaudhary[b], Edward N. Matteo[a], M. Bayani Cardenas[b], Randall T. Cygan[a]

[a] Sandia National Laboratories, Albuquerque, NM, United States
[b] University of Texas, Austin, TX, United States

ARTICLE INFO

Keywords:
Molecular dynamics
Carbon dioxide
Sequestration
Muscovite
Contact angle
Adsorption

ABSTRACT

Capture and subsequent geologic storage of CO_2 in deep brine reservoirs plays a significant role in plans to reduce atmospheric carbon emission and resulting global climate change. Subsurface injection of CO_2 is also used industrially in enhanced oil and natural gas recovery operations to increase the amount of hydrocarbon that can be economically recovered from a geologic reservoir. The interaction of CO_2 and brine species with mineral surfaces controls the ultimate fate of injected CO_2 at the nanoscale via surface chemistry, at the pore-scale via capillary trapping, and at the field-scale via relative permeability. High resolution micro X-ray CT scanning, optical contact angle measurements, and large scale molecular dynamics simulations were used to investigate the behavior of supercritical CO_2 and aqueous fluids on basal surfaces of muscovite, a common phyllosilicate mineral. Experimental results demonstrate partial wetting by the aqueous phase and a dependence of contact angle upon aqueous phase brine composition. This contrasts with simulation results, which predict that supercritical CO_2 forms a non-wetting droplet, separated from direct interaction with the muscovite surface by distinct layers of water and charged species. Simulations with trace amounts of acetate or acetic acid added to the CO_2/water/mineral system were used to investigate the potential effect of contamination with small organic molecules. While the observed contact angle was not significantly altered, these simulations demonstrate the influence of pH on species partitioning, with acetic acid molecules partitioning to the CO_2/water interface and acetate ions adsorbing to the mineral surface. Similar simulations using hexanoate displayed a greater surfactant effect and significantly increased wetting by the CO_2 phase, suggesting that small concentrations of secondary species or contaminants can significantly influence macroscopic wetting behavior.

1. Introduction

Capture and subsequent geologic storage of CO_2 in deep brine reservoirs plays a significant role in plans to reduce atmospheric carbon emission and resulting global climate change (Metz, 2005). Evaluation and implementation of proposed scenarios for injecting CO_2 into sedimentary reservoirs requires understanding the interactions between supercritical CO_2, aqueous brines, and the mineral phases found in the reservoir and overlying caprock. In particular the relative wetting of pore surfaces in the rock matrix by CO_2 and brine, characterized macroscopically by contact angles, controls the capillary pressure of the fluids in the pore and strongly influences the transport and ultimate distribution of CO_2 in the reservoir (Saadatpoor et al., 2010; Krevor et al., 2011). Knowledge of meso- and molecular-scale interactions between fluid and mineral phases can be used to develop larger-scale conceptual models for multi-phase surface wetting to help evaluate the fate of supercritical CO_2 in the reservoir (Wang et al., 2013; Parmigiani et al., 2011).

Wettability of supercritical CO_2 in subsurface aquifers is of interest for storage efficiency and leakage concerns during geologic carbon storage (GCS) (Iglauer et al., 2015). Because of the ubiquity of clay minerals in both reservoir and caprock lithologies, many researchers have examined wettability in brine-muscovite-CO_2 systems as muscovite surfaces are similar in molecular structure to clay mineral surfaces to act as a proxy for clay mineral wettability. Experimental studies have been conducted to determine the wettability of caprock and reservoir materials in CO_2–brine systems (Chiquet et al., 2007, 2007; Espinoza and Santamarina, 2010; Bikkina, 2011; Kim et al., 2012; Saraji et al., 2013), but reported wetting trends with respect to temperature, pressure, and brine composition are not always consistent (Heath

* Corresponding author.
E-mail address: cmtenne@sandia.gov (C.M. Tenney).

http://dx.doi.org/10.1016/j.petrol.2016.10.010
Received 29 February 2016; Received in revised form 23 September 2016; Accepted 4 October 2016
Available online 05 October 2016
0920-4105/

et al., 2012; Mahadevan, 2012).

Iglauer et al. and Wan et al. provide a review of literature on muscovitebrine-CO_2 wettability, and show a large range in contact angles as a function of conditions (temperature, pressure, and ionic strength) (Iglauer et al., 2015; Wan et al., 2014). In general previous works report increases in wetting phase (water) contact angles in mica systems with increasing pressure and with greater contact time between CO_2 and mica surfaces (up to 50 days) (Wang et al., 2013; Chiquet et al., 2007; Wan et al., 2014; Broseta et al., 2012; Farokhpoor et al., 2013). Advancing contact angles can range up to 100°, while receding angles are much less (perhaps ~20°) (Wan et al., 2014; Broseta et al., 2012). Static contact angles obtained by workers have intermediate values with somewhat less scatter showing consistent increases with pressure (Wan et al., 2014; Farokhpoor et al., 2013).

Progressive reaction of muscovite surfaces results in alteration and surface roughening which appears to favor CO_2 wettability and increases in wetting phase contact angle (Wan et al., 2014). Much has been made in the literature concerning surface treatments and potential contamination and the collective influence on wettability measurements. Iglauer et al. (2014) address contamination and cleaning effects on silica surfaces and propose cleaning all surfaces with strongly oxidizing solutions prior to measurement to ensure surfaces are contaminant free. Saraji et al. (2014) suggest that such cleaning may alter surface properties of silicate minerals, creating an artificial hydrophobicity.

Ionic strength effects on wettability are well known from oil field, environmental, and soil literature (Buckley, 2001; Jr et al., 1997; Leelamanie and Karube, 2013) as well the GCS literature (Wan et al., 2014; Farokhpoor et al., 2013; Jung and Wan, 2012). In CO_2-brine-silicate mineral systems, a general increase in contact angle with ionic strength is noted (Farokhpoor et al., 2013; Jung and Wan, 2012) but other authors have noted very little or uncertain influence (Chiquet et al., 2007; Wan et al., 2014; Broseta et al., 2012). No literature exists on the potential influence of various cations in mica wettability in CO_2 systems, although a slight difference is noted when using, e.g., $CaCl_2$ vs NaCl in other systems (Jr et al., 1997; Leelamanie and Karube, 2013). In this work, we examine wettability variations in brine-CO_2-muscovite systems as a function of ionic strength with attention to any potential divalent vs monovalent cation effects. We present new experimental results that show a slight increase in wettability with ionic strength with little or no difference noted as a function of cation content.

A contact angle θ_C is defined here as the angle formed between the interface of a droplet and solid surface and the interface of the droplet and the surrounding bulk fluid phase (see Fig. 1). For wetting fluids $\theta_C < \pi/2$ and for non-wetting fluids $\theta_C > \pi/2$. As described by Young's equation,

$$\gamma S1 = \gamma S2 + \gamma 12 cos\theta C \quad (1)$$

the equilibrium contact angle results from the balance of forces between the interfacial tensions (or surface free energies) γ_{ij} between two fluids (subscripts 1 and 2) and a solid surface (subscript S). Note that this definition and Eq. (1) only truly apply to macroscopic systems, and complications may arise when contact angle is considered at the nanoscale. For example, as droplet size decreases, the free energy associated with creating the three-phase contact line may become significant and needs to be added to Eq. (1) (Amirfazli and Neumann, 2004; Tadmor, 2008; Brinkmann et al., 2005). Also, near the three-phase line molecular interactions between two phases can be altered by the presence of the third phase, resulting in a local nanoscale contact angle that may differ from its macroscopic value. While the simulation work described in this paper is primarily concerned with general wetting trends and details of molecular ordering at interfaces, we attempted to minimize the potential for nano- versus macro-scale complications by simulating relatively large systems with cylindrical, as opposed to spherical, droplet geometries. The systems used in this study are described in greater detail in the next section. For the purposes this paper, we will generally assume an interpretation of contact angle akin to that depicted in Fig. 1.

In this study we used molecular dynamics simulations (Plimpton, 1995; Plimpton) to investigate interfacial behavior and evaluate contact angles for CO_2-brine-mineral systems.

Previous studies of contact angles using molecular simulation include water on graphene (Taherian et al., 2013; Sergi et al., 2012; Scocchi et al., 2011), water and surfactant on hydrocarbon surfaces (Halverson et al., 2009), water on gold (Wu et al., 2012), epoxy on SiO_2 (Holck et al., 2012), CO_2 and brine on quartz (Iglauer et al., 2012), water on kaolinite (Solc et al., 2011), and CO_2 and brine on kaolinite (Tenney and Cygan, 2014). Molecular simulation has also been used to study interfacial tension in CO_2-water systems (Nielsen et al., 2012; Li et al., 2013). Accurate interatomic potentials (Cygan et al., 2004; Cygan et al., 2012) were used to evaluate the energy and forces associated with hundreds of thousands of atoms for various fluid droplet configurations within slit pores formed between basal surfaces of muscovite, a common phyllosilicate mineral. Clay and clay-like minerals are present in many potential sites being considered for carbon sequestration, where these phases occur as coatings on sandstone grains and as the dominant mineral phase of shale caprocks. Muscovite is easily cleaved to expose relatively uniform and hydrophilic basal surfaces that are suitable for experimental determinations of contact angles, which allows relatively easy comparison with simulation results. In addition to providing the foundational science for understanding the molecular control in wetting processes, such results can be used to improve capillary flow and capillary trapping models to better assess the disposition of CO_2 in sequestration reservoirs.

2. Experimental details

2.1. Micro X-ray CT scanning

The wetting characteristics of muscovite/CO_2/brine systems were investigated by laboratory experiments to quantify the contact angle θ_C (Eq. (1)). A novel experimental technique was developed using high resolution micro X-ray CT scanning for imaging the interface of fluids with a solid surface (Chaudhary et al., 2015). Rectangular chips (20 mm×7 mm) of muscovite were oriented in a parallel-plate arrangement and vertically placed inside a PEEK column (7.5 mm ID) heated with a carbon fiber sleeve (Fig. 2). Temperature was maintained at 333 K and pressure at 13.8 MPa. Three different aqueous phase salt concentrations (100% DI-water, 1.26 wt% $CaCl_2$ brine, and 2.00 wt% NaCl brine) were used. In addition, 1.00 wt% NaBr was used to enhance the image contrast during X-ray CT scanning. The column was pressurized with brine and CO_2 and allowed 4 h of dissolution-equilibration time. The column was scanned using an Xradia MicroXCT-400 scanner, which provided images of the CO_2-brine interface with muscovite surfaces. The spacing between the parallel muscovite chips was optimized based on the Bond Number B_o given as

$$B_o = \frac{(\Delta\rho)gL^2}{\gamma} \quad (2)$$

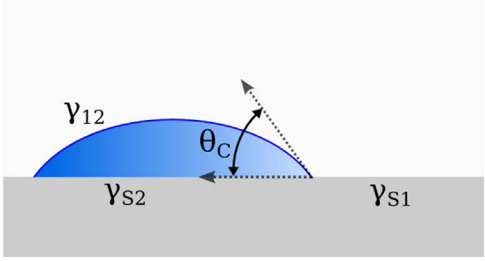

Fig. 1. Contact angle θ_C resulting from the balance of forces between interfacial tensions γ_{ij} between two fluids (subscripts 1 and 2) and a solid surface (subscript S).

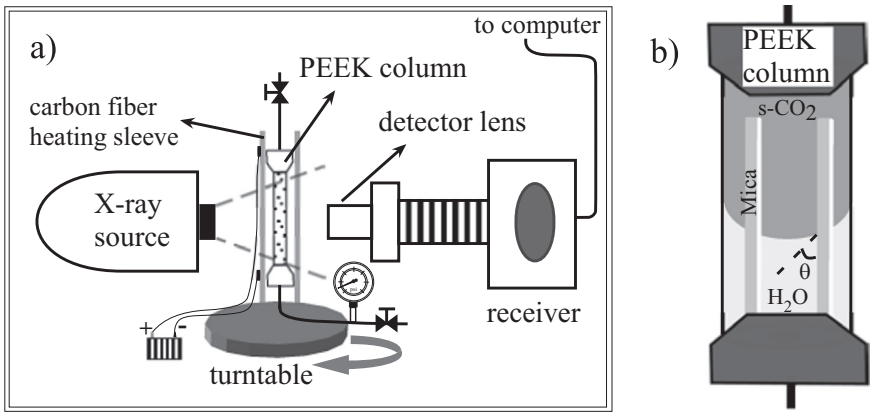

Fig. 2. (a) A diagram of the micro X-ray CT scanning set-up for imaging PEEK column, and (b) a diagram showing the orientation of parallel muscovite chips inside the PEEK column with supercritical carbon dioxide (s-CO_2) and brine.

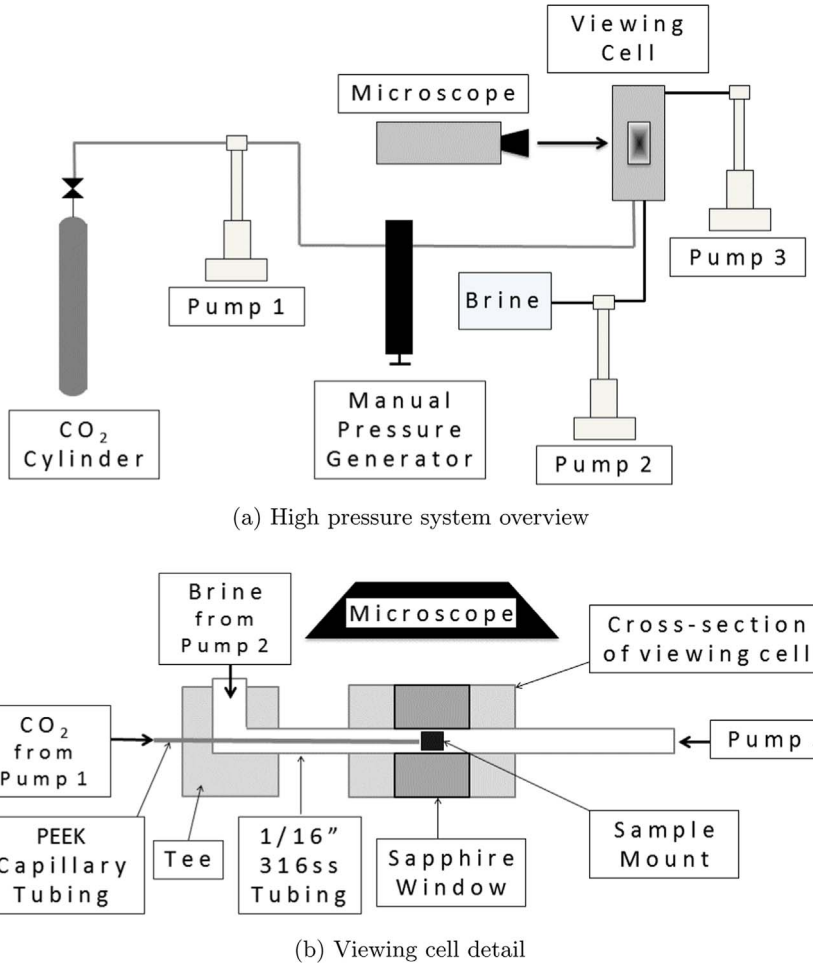

Fig. 3. (a) High pressure system used to prepare and image contact angles in the brine-CO_2muscovite system. Two ISCO syringe pumps are used to meter and maintain pressure for CO_2 (Pump 1) and brine (Pump 2), while a third pump (Pump 3) was used to provide backpressure. A Zeiss Stemi Sv-11 Apo stereo microscope together with a Harrick high pressure demountable liquid cell with sapphire windows permitted viewing of CO_2 wetting behavior at 13.8 MPa and 60 °C. (b) A thin PEEK capillary tube was placed inside a 1.59 mm 316ss high pressure capillary tube attached to the view cell for metering and control of CO_2 drop size. (a) High pressure system overview. (b) Viewing cell detail.

where $\Delta\rho$ is the density difference between the CO_2-brine fluid pair, g is acceleration due to gravity, L is the spacing between the muscovite chips, and γ is the interfacial surface tension of the fluids. The spacing of 1 mm between the parallel muscovite chips results in $B_o < 0.1$ and ensured the interface had negligible effect due to gravity. When the surface tension forces are dominant, i.e., $B_o < 1$, interface of fluids will follow the arc of a circle, and a tangent to this circle at the contact of linear muscovite surface gives the contact angle θ_C. Contact angle was measured digitally by using the image processing program ImageJ.

2.2. Optical contact angle measurement

Imaging of supercritical CO_2 contact angles on mica surfaces utilized a Harrick high pressure demountable liquid cell with sapphire windows, suitable for pressures to 34.5 MPa and temperatures to 240 °C. We used ethylene propylene o-rings to ensure a quality

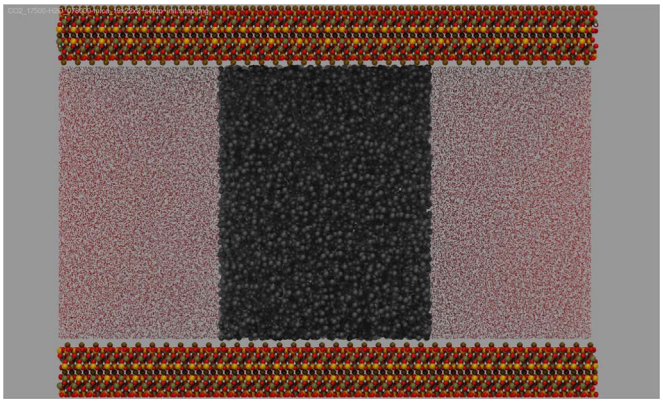

Fig. 4. Initial configuration of an infinitely long CO_2 "droplet" (System 2 in Table 1) surrounded by water in a slit pore formed between basal surfaces of muscovite. Aluminum, silicon, oxygen, and hydrogen atoms within the muscovite slab are represented as tan, orange, red, and white spheres, respectively. Interlayer potassium ions are shown as brown spheres. Within the fluid-filled slit pore, black spheres are CO_2 carbon atoms and red dots are H_2O oxygen atoms·H_2O hydrogen atoms are omitted for clarity. Atoms represented as spheres are rendered at 60% of their van der Waals radii.

Table 1
CO_2-brine-mineral simulation systems described in this study.

			Number of molecules		
System	T/K	P/MPa	CO_2	H_2O	solute
1	333	13.8	17500	104000	–
2	333	13.8	17500	78000	–
3	333	13.8	17500	52000	–
4	333	13.8	17500	52000	108 $CaCl_2$
5	333	13.8	17500	52000	570 $CaCl_2$
6	333	13.8	17500	52000	327 NaCl
7	333	13.8	17500	52000	1781 NaCl
8	333	13.8	17500	52000	400 CH_3COOH
9	333	13.8	17500	52000	400 $NaCH_3COO$

pressure seal while maintaining compatibility with CO_2. Separate ISCO syringe pumps maintained pressures for the two fluid phases, and pressure relief valves fitted with ethylene propylene o-rings protected against accidental overpressure (Fig. 3A). A 510 μm outer diameter (OD) by 255 μm inner diameter (ID) poly –ether-ether ketone (PEEK) capillary tube fit inside a 1.59 mm OD by 0.762 mm ID stainless steel capillary tube attached to a manual pressure generator (Fig. 3B) was used to meter and control CO_2 bubbles within the liquid cell, with the annular space between the PEEK and steel tubing used to meter brine solution within the cell (Fig. 3B).

Fresh muscovite samples were collected from the Ingersoll mine, South Dakota, USA and determined to have the composition (K0.90Na0.08)(Al2.91Fe0.12Mn0.01Si2.96O10)(OH1.83F0.17) by electron microprobe facilities at the University of New Mexico (Michael Spelde, Personal Communication, 2013). Rectangular muscovite samples approximately 2 mm by 4 mm were carefully prepared by trimming with stainless scissors and mounted on titanium flats using Sylgard 184 silicone elastomer epoxy cured for 1 h at 60 °C, followed by a 24-h cure inside a desiccator. The titanium flats were mounted inside round hastelloy cells 2 mm wide and 0.31 mm ID, giving a nominal cell internal volume (minus the sample) of 0.25 cm^3. Utensils and mounting hardware were cleaned by first soaking in acetone for 30 min, followed by isopropanol for 30 min, then washed and triple rinsed in 18MΩ RO deionized water.

In a few examples we measured dynamic contact angles by slightly increasing and decreasing the bubble size by use of the manual pressure generator, which allowed for the determination of advancing and receding contact angles by manually forcing in and withdrawing CO_2 from the liquid cell chamber. Just prior to measurement, a freshly cleaved surface was obtained using a stainless steel blade. Prior to imaging, the bubble was allowed to rest for up to four hours which ensured that equilibration between the internal brine solution and CO_2 was achieved prior to imaging. Our SEM imaging of mica surfaces shows microscopically smooth surfaces with only a few steps, which suggests that surface roughness had little to no effect on observed contact angles.

Aqueous solutions were initially prepared using 18MΩ RO deionized water and reagent grade salts of NaCl and $CaCl_2$ bubbled with ultrapure CO_2 at room temperature and pressure in Nalgene vessels. Prior to use, the interior of the syringe pumps and all high pressure tubing was rinsed in isopropyl alcohol followed by four volumes of 18MΩ RO deionized water. The sample cell was flushed with four volumes of aqueous solution and then brought to 60 °C and 13.8 MPa pressure with cell backpressure being provided by a third ISCO syringe pump (Fig. 3). The cell was then flushed with four volumes of CO_2, before being filled with the aqueous solution at pressure. A single bubble approximately 0.05 cm^3 was then metered onto the mica surface via the PEEK capillary tube. In most cases the bubble was held "captive" by the peek tubing/pressure generator assembly and allowed to equilibrate with the aqueous solution prior to measurement. In a few examples we measured dynamic contact angles by slightly increasing and decreasing the bubble size by use of the manual pressure generator, which allowed for the determination of advancing and receding contact angles by manually forcing in and withdrawing CO_2 from the liquid cell chamber. The bubble was allowed to rest for up to four hours prior to imaging, to ensure that equilibration between the internal brine solution and CO_2 was achieved. Images of CO_2 droplets were taken with a Zeiss Stemi Sv-11 Apo stereo microscope and Zeiss Axiovision software. Contact angles were measured using ImageJ (Ferreira and Rasband, 2012) with the DropSnake plugin (Stalder et al., 2010). Raw digital images obtained from the software were converted to 8-bit grayscale, cropped,

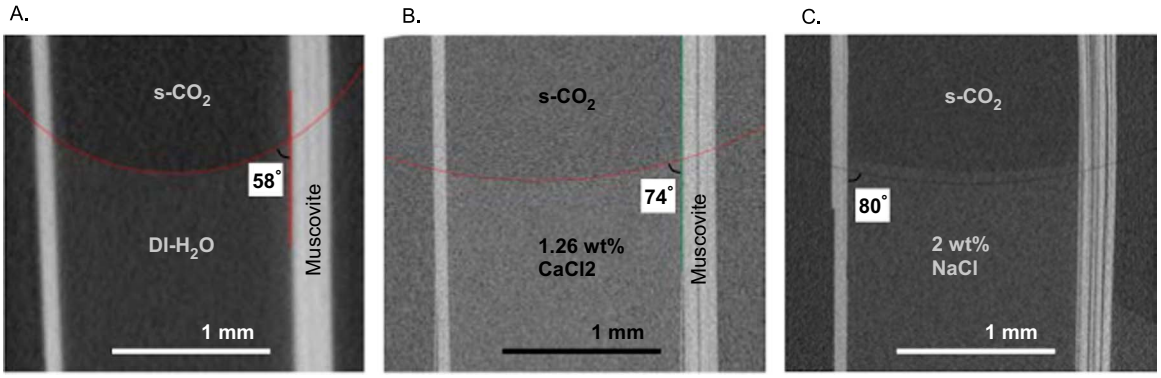

Fig. 5. Images showing the measured contact angles of CO_2/brine/muscovite systems with an aqueous phase of A) DI water, B) 1.26 wt% $CaCl_2$ brine, and C) 2.00 wt% NaCl brine at 16.8 MPa and 333 K. Note that in C) the circular arc tracking the interface of fluids is lowered to show the interface in raw image.

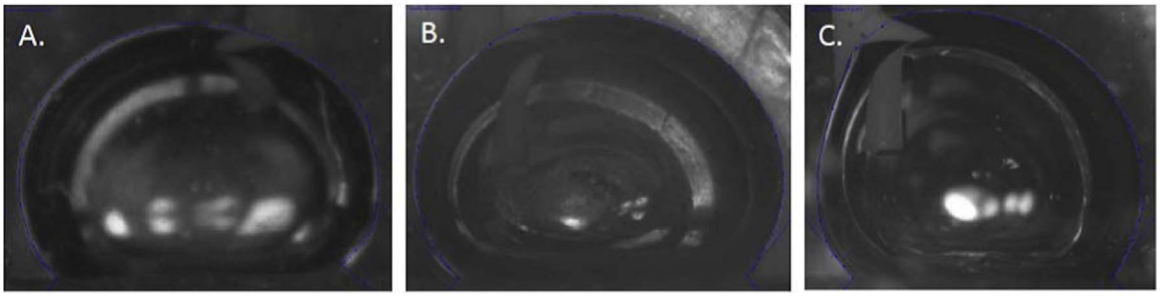

Fig. 6. Images of CO_2 droplets contacting fresh muscovite surfaces (images are inverted) in aqueous solutions. These examples show A. Deionized water. B. 2.00 wt% NaCl solution (0.625 mol% or 0.034 molal NaCl). C. 1.26 wt% $CaCl_2$ (0.21 mol% or 0.01 molal $CaCl_2$). Water contact angles (q) ranging from (45 ± 2)° (A), (52 ± 2)° (B) and (54 ± 3)° (C) all show water-wet behavior.

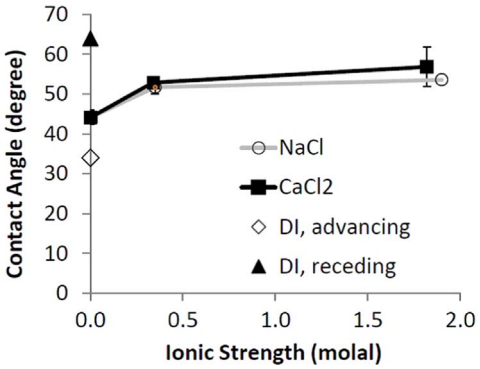

Fig. 7. Variations in static and dynamic contact angles in the CO2-brine-muscovite system, plotted as the wetting phase angle, θ.

rotated vertically and enhanced for contrast prior to analysis.

SEM images of muscovite surfaces were obtained using a TESCAN Vega3 LMU tungsten filament scanning electron microscope operated at 20 kV accelerating voltage in low vacuum mode with 15 Pa N2. Micrographs were collected using an annular YAG scintillator back-scatter electron detector.

3. Simulation details

Muscovite was chosen as the model mineral surface for this study because it provides a relatively simple substrate for studying surface adsorption, due to the ease with which it can be cleaved to expose relatively clean and uniform basal surfaces. Muscovite ($KAl_2(AlSi_3O_{10}(OH)_2$) is a three-sheet phyllosilicate mineral. The inner sheet is made up of AlO_6 octahedra and the outer sheets SiO_4 tetrahedra with Al atoms replacing one out of four Si atoms, resulting in a net negative charge. Layers are held together by electrostatic forces, with interlayer cations (e.g. K^+) providing charge balance. Fig. S1 in the Supporting Information shows the structure for a muscovite unit cell. The basal muscovite surface is hydrophilic. The systems studied in this work focus solely upon the basal surfaces of muscovite. Carbon dioxide is expected to be more reactive at muscovite edges, where protonation-deprotonation reactions with the brine or CO_2 fluid can control reactions with the mineral. While it is known that charge density on the basal surfaces of minerals can vary with pH (Gupta and Miller, 2010), we did not attempt to explicitly account for this, and instead allowed the initial, experimentally-derived crystal structure (Catti et al., 1994) to relax and adsorb fluid species as dictated by the simulation force field.

Fig. 4 shows the initial configuration used for the simulation of a CO_2 droplet and water located within a slit pore formed between the basal surfaces of muscovite. The simulation cell contains a four-layer slab of muscovite (approximately 4 nm thick) with fluid located adjacent to the basal surfaces. For the droplet shown in Fig. 4, periodic boundary conditions result in an infinitely long droplet or filament. Cylindrical droplet geometries have been used previously for determination of contact angle via molecular simulation and study of the effects of the three-phase line tension (Scocchi et al., 2011). A cylindrical droplet geometry was chosen in favor of conventional spherical geometry to reduce two potential scale effects. First, use of cylindrical geometry reduces droplet curvature, which reduces the pressure differential across the liquid-liquid interface of these nanoscale droplets, which improves the match between nano- and macroscale pressures interior to the droplet. Second, use of cylindrical geometry eliminates the influence of the three-phase line tension, which can significantly influence contact angle results at small length scales (Amirfazli and Neumann, 2004; Tadmor, 2008; Brinkmann et al., 2005). Previous simulations using spherical droplets (not shown) showed no preferential wetting direction on the basal surface of muscovite, and the effect of different orientations of the cylindrical

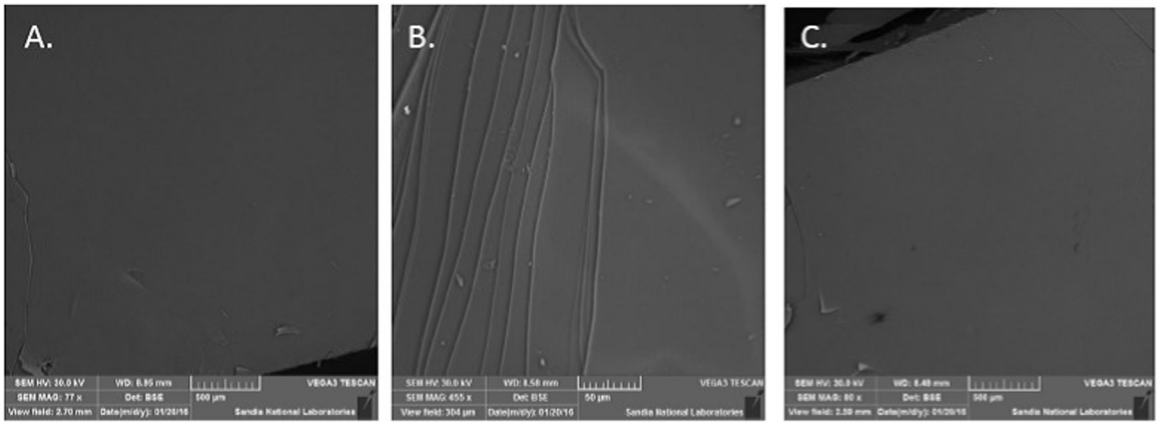

Fig. 8. Muscovite surfaces used in this study examined via a variable pressure SEM. A. A freshly cleaved surface similar to ones used as experimental starting materials. B. Muscovite surface exposed to a 2% NaCl solution for four hours. C. Muscovite surface exposed to 6.3% $CaCl_2$ solution for four hours. Scale bars for A and C are 500 μm; scale bar for B is 50 μm.

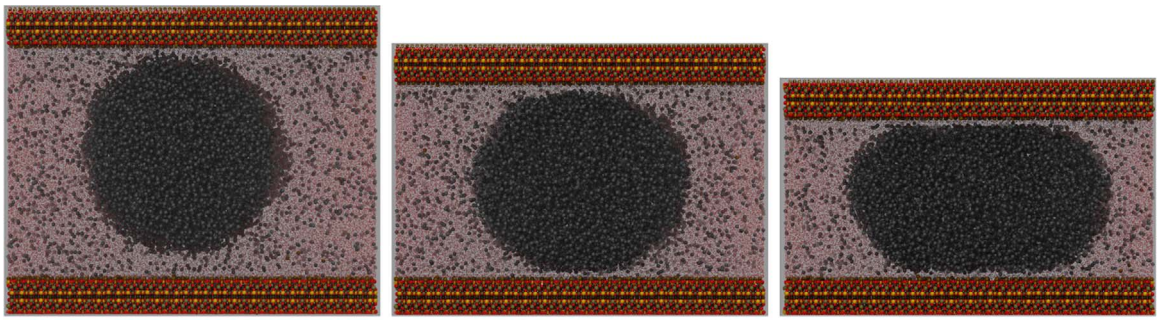

Fig. 9. Final snapshots of CO_2 and water in muscovite slit pores. Subfigure captions refer to the simulation systems described in Table 1. The number of H_2O molecules was varied, while holding CO_2 and muscovite components constant, to yield different slit pore widths (approximately 12 nm, 10 nm, and 8 nm). Aluminum, silicon, oxygen, and hydrogen atoms within the muscovite slab are represented as tan, orange, red, and white spheres, respectively. Interlayer potassium ions are shown as brown spheres. Within the fluid-filled slit pore, black spheres are CO_2 carbon atoms and red dots are H_2O oxygen atoms·H_2O hydrogen atoms are omitted for clarity. Atoms represented as spheres are rendered at 60% of their van der Waals radii. (a) System 1. (b) System 2. (c) System 3.

droplet axis was not explored.

Similar initial configurations were used for most of the systems described in this paper. These other systems may include the use of NaCl or $CaCl_2$ brines instead of pure water. Table 1 summarizes the CO_2-brine-mineral simulation systems referred to in this paper. Na^+, Ca^{2+}, and Cl^- are the most common ionic constituents found in deep brine reservoirs of interest for CO_2 sequestration (Wunsch et al., 2013). Simplified NaCl and $CaCl_2$ brines were used in this study to isolate the behavior of monovalent and divalant cations. Brine compositions were chosen to result in a range of ionic strengths.

Systems were simulated at temperatures of 330 K or 333 K and pressures of 20 MPa or 13.8 MPa, which is above the critical point for carbon dioxide and represents realistic temperature and pressure conditions for deep saline reservoirs. At least 10 ns of simulation time was allowed for systems to reach equilibrium. Total simulation times varied from approximately 15 ns to approximately 30 ns. Further details regarding the methods and parameters used for simulation and analysis in this study can be found in the Supporting Information.

4. Results and discussion

4.1. Micro X-ray CT scanning

High-resolution X-ray CT scanning of the column set-up shown in Fig. 2 provided images with distinct fluid pair and mineral interfaces (Fig. 5) for CO_2/brine/muscovite systems. Given negligible gravity effects, the curvature of the interface followed a circular arc. The aqueous fluid contact angle θ_C in presence of CO_2 was measured to be 58° for DI water, 74° for 1.26 wt% $CaCl_2$ brine, and 80° for 2.00 wt% NaCl brine at 333 K and 16.8 MPa The observed contact angles indicate that muscovite is water-wet relative to CO_2, particularly in the case of DI water. The addition of salt decreases CO_2 wetting slightly, as indicated by an approximately 20° increase in the contact angle. Similar intermediate-wet characteristic for mica is also noted by other studies (Chiquet et al., 2007; Heath et al., 2012; Broseta et al., 2012). Chiquet et al. (2007) report that increasing the salt concentration from 0.01 M NaCl to 1 M NaCl increases the contact angle on mica surface by approximately 25°. Given that most subsurface storage aquifers have some native salinity, muscovite with an aqueous fluid contact angle of approximately 80° will exhibit intermediate-wet characteristics in natural setting.

4.2. Optical contact angle measurement

CO_2-muscovite-brine contact angles are shown for example droplets in Fig. 6 and plotted as functions of ionic strength in Fig. 7. Here we report contact angles as those of the aqueous phase, θ, which are related to measured values using CO_2 droplets, α, as θ=180° − α (Iglauer et al., 2015). This range in values is similar to sessile drop measurements by Wan et al. (2014) at similar pressure. These observed wetting trends are qualitatively consistent with those in the X-ray CT scanning results described in Section 4.1. The relatively higher water contact angles observed in the X-ray CT experiments could be due to differences in muscovite samples, differences in preparation techniques, or the addition of 1% NaBr for improved X-ray contrast. To approximate conditions of the molecular dynamics simulations, we only used freshly cleaved muscovite surfaces and limited exposure times to between 30 min and 4 h. This was done to avoid potential aging effects as discussed by Wan et al. (2014). All values of contact angle show water-wetting behavior, with a small increase as a function of ionic strength (Fig. 7) noted for both NaCl and $CaCl_2$ solutions. The increase with ionic strength appears to be greatest at the lowest ionic strength for both solutions, with little change evident between 0.3 and 1.8 molal ionic strengths. We observed no measurable difference between the different cations. Dynamic measurements of contact angle measured in distilled water show a larger variation (34° for advancing and 64° for receding), which falls within the range given in the summary for muscovite surfaces by Iglauer et al. (2015) for similar pressures. Although Wan et al. (2014) note no systematic change with ionic strength for freshly cleaved muscovite, our values are close to those reported for the sessile drop method at similar pressures by those authors.

4.3. Muscovite surface alteration

To examine the state of the freshly cleaved muscovite prior to and after exposure to brine and CO_2, we examined example surfaces using a variable pressure SEM (Fig. 8). All surfaces lack any signs of noticeable alteration or deformation at edges associated with sample preparation. Small micron –sized steps such as those seen in Fig. 8B may be responsible for the variation in dynamic advancing and receding contact angles plotted in Fig. 7. Higher resolution images (not shown) did not show any indication of the micron-sized blisters associated with decompression on muscovite surfaces discussed by Wan et al. (2014).

4.4. Molecular simulation

Fig. 9 shows snapshots of infinitely long cylindrical supercritical CO_2 droplets surrounded by an aqueous phase of water and dissolved CO_2 confined within muscovite slit pores of various widths (approximately 12 nm, 10 nm, and 8 nm) at 333 K and 13.8 MPa. Fig. 10 shows the time- and space-averaged densities of H_2O and CO_2 for the same systems. In all cases the CO_2 phase is strongly non-wetting. For the largest slit pore, the CO_2 bubble detaches from the pore wall and

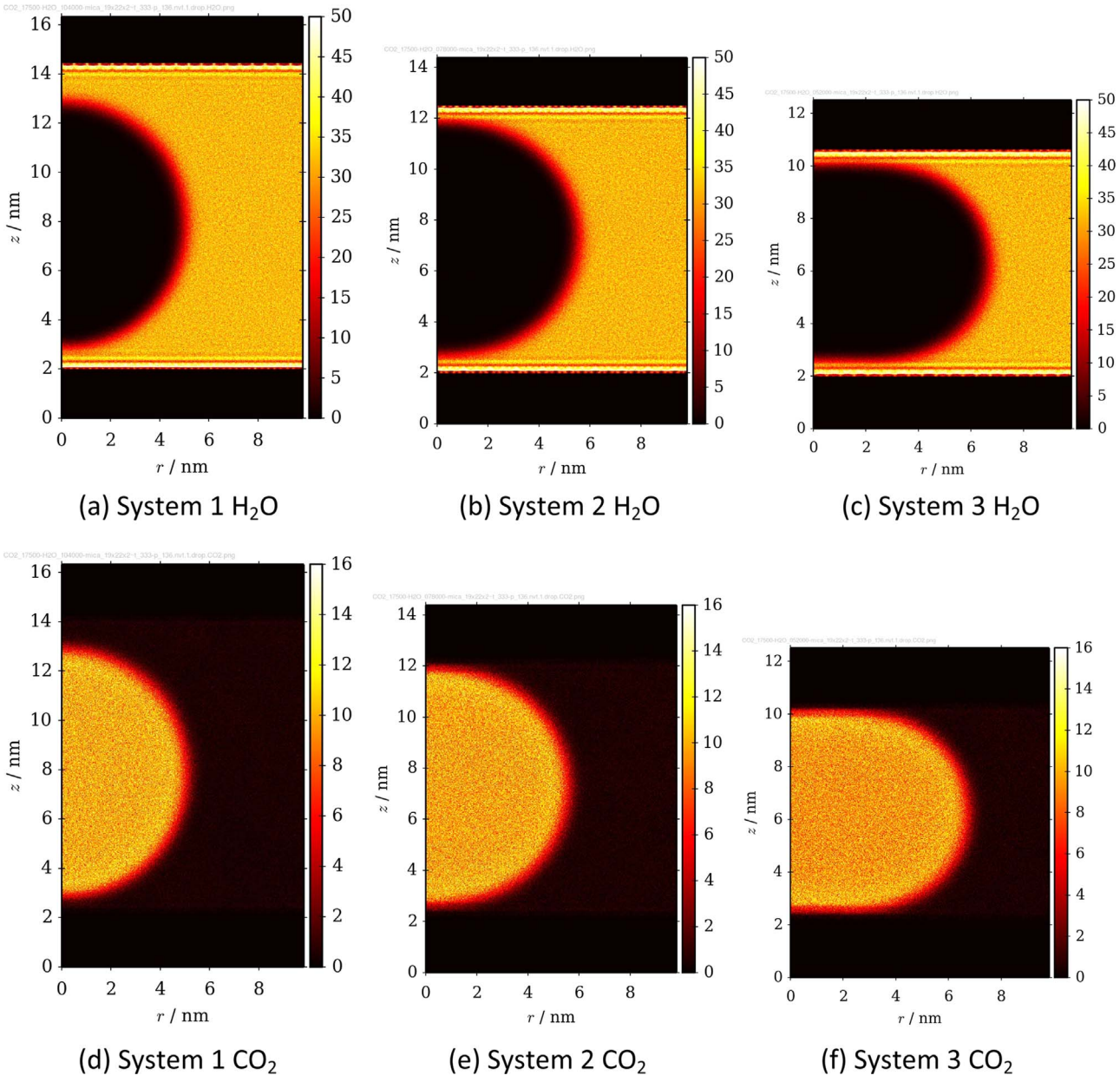

Fig. 10. Densities of H_2O (top) and CO_2 (bottom) averaged over the final 2 ns of simulation around and along the plane of (approximate) system symmetry passing through the long axis of the CO_2 droplet. Subfigure captions refer to the simulation systems described in Table 1. Densities vary from 0 (black), through intermediate values (red to yellow), to the maximum value observed in the system (white). Density values are in units of molecules per nm^3. Two layers of muscovite occupy the zone from z=0 to approximately z=2; similarly for the top ~2 nm of each figure. (a) System 1H_2O. (b) System 2H_2O. (c) System 3H_2O. (d) System 1 CO_2. (e) System 2 CO_2. (f) System 3 CO_2.

maintains a circular cross section; but as pore width decreases, the CO_2 bubble is increasingly confined. The pressure exerted by a non-wetting CO_2 bubble upon the confining slit pore wall will increase as pore width decreases, due to droplet curvature and resulting capillary pressure effects. Muscovite K^+ ions remain strongly adsorbed to the (negatively charged) mineral surface, with very few dissolving into the bulk aqueous phase. Given the strongly charged nature of mineral–fluid interface for these model systems, preferential adsorption of water relative to CO_2 is observed, and the CO_2 droplets in all slit pores are clearly separated from mineral surfaces by a thin, dense water layer (Fig. 10). A second, much more diffuse water layer between the droplet and mineral surface is also clearly evident in Fig. 10a, but this layer is disrupted slightly by the confined bubble in Fig. 10c. Although the extent of water adsorption under the CO_2 bubble changes as the bubble is confined, the CO_2 droplet contact angle does not change noticeably under these simulation conditions. Similar simulations at 330 K and 20.0 MPa showed no appreciable change in adsorption or wetting behavior; the CO_2 phase remains strongly non-wetting.

Replacing water with brine in the simulation system does not change the strongly non-wetting character of CO_2. Fig. 11 shows the time- and space averaged densities of H_2O and brine species for systems composed of infinitely long supercritical CO_2 droplets surrounded by 6.33 wt% $CaCl_2$ or 10.00 wt% NaCl brine confined within muscovite slit pores of approximately 8 nm width at 333 K and 13.8 MPa. Significant adsorption of water, cations, and anions at the mineral surface is evident. Fig. 11b shows Ca^{2+} interacting with the mineral surface very slightly below and partly within the first layer of adsorbed water molecules (Fig. 11a). The highest density of Cl^- anions (Fig. 11c) in this system occurs just beyond this layer of Ca^{2+}. This contrasts with the behavior seen in Fig. 11e, which shows a layer of Na^+ interacting more directly with the mineral surface, distinctly below the first adsorbed water layer (Fig. 11d). A second layer of adsorbed Na^+

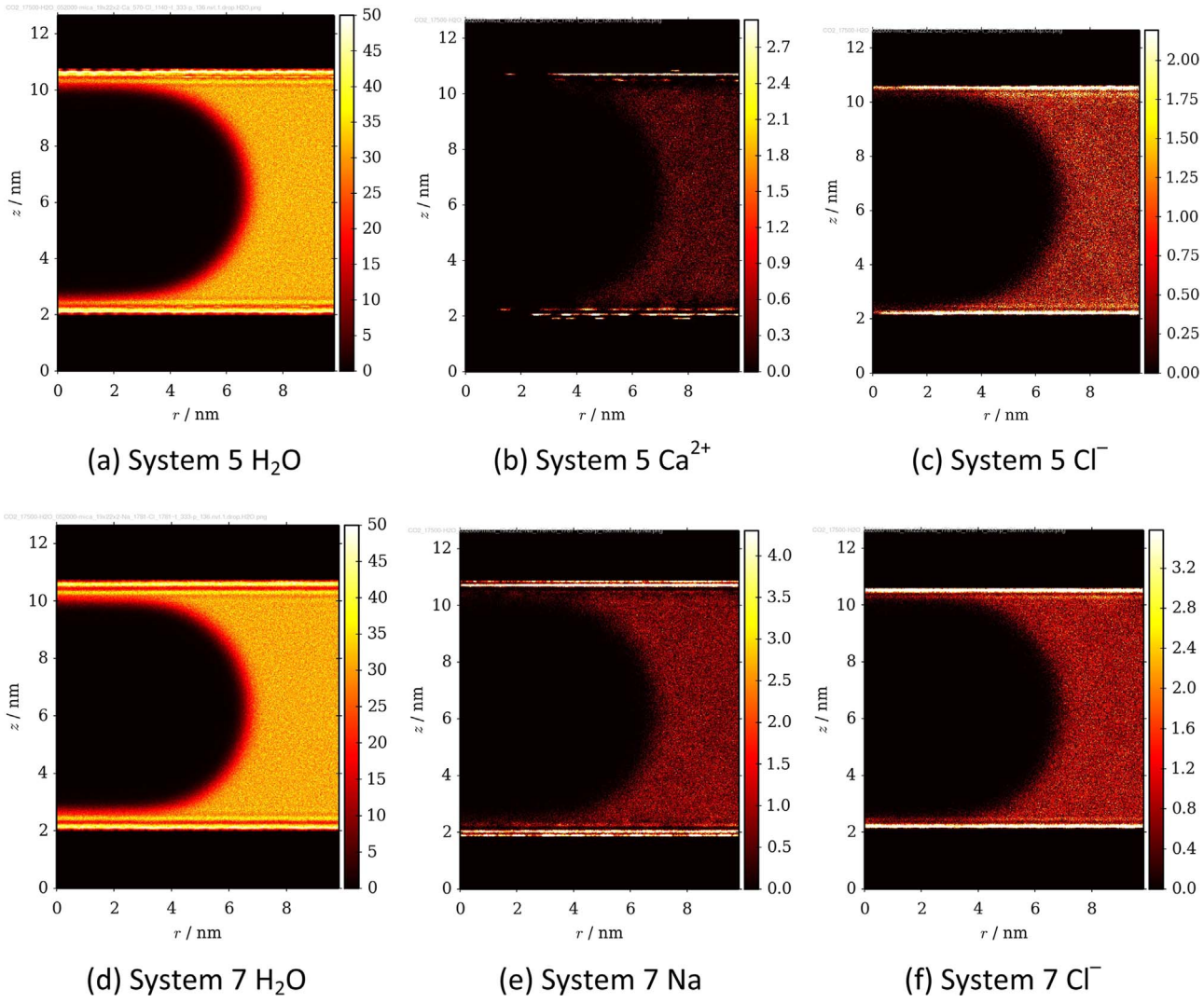

Fig. 11. Densities of H_2O and brine ions averaged over the final 2 ns of simulation around and along the plane of (approximate) system symmetry passing through the long axis of the CO_2 droplet. Notation as in Fig. 10. (a) System 5H_2O. (b) System 5 Ca^{2+}. (c) System 5 Cl^-. (d) System 7H_2O. (e) System 7 Na. (f) System 7 Cl^-.

occurs at the same level observed for the Ca^{2+} and first adsorbed H_2O layer. Cl^- density (Fig. 11f) is again highest just outside this second Na^+ layer. The relative adsorption behavior of Ca^{2+} and Na^+ is consistent with their hydration energies, where the divalent cation prefers coordination by water molecules, rather than adsorbing more directly to the surface as Na^+ does in these simulations.

Comparison of Figs. 10c and 11d suggests that the presence of Na^+ and Cl^- ions strengthen the ordering of H_2O molecules in the second, relatively diffuse layer of H_2O adsorbed to the muscovite surface. As mentioned above, pressure from the confined CO_2 bubble appears to disrupt this diffuse H_2O layer (Fig. 10c), but it is again clearly present in Fig. 11d. This apparent enhanced ordering was not observed for the 6.33 wt% $CaCl_2$ brine system (Fig. 11a), nor for the weaker 2.00 wt% NaCl brine system (not shown). Aside from this ordering of the diffuse water layer in the 10.00 wt% NaCl brine system, simulations of the weaker 1.26 wt% $CaCl_2$ or 2.00 wt% NaCl brine systems (see Table 1) yielded results generally similar to those observed in the more concentrated systems and are not shown.

The adsorption of $CaCl_2$ brine species on muscovite differs significantly from behavior observed in prior work (Tenney and Cygan, 2014) studying adsorption on the hydrophilic surface of kaolinite. Specifically, the hydrophilic surface of kaolinite, which is uncharged and covered with hydroxyl groups, showed the most prominent layer of Ca^{2+} interacting with the mineral surface only *through* a lower layer of intermediate water molecules. Further, the highest density of Cl^- anions in the kaolinite system occurred *between* the mineral surface and the layer of Ca^{2+}, not outside as in the present muscovite case. Unlike $CaCl_2$ brines, adsorption behavior for NaCl brines was similar on muscovite and hydrophilic kaolinite surfaces. Although in all of these cases the macroscopic wetting behavior is relatively consistent, the molecular scale details differ significantly, which may have implications, for example, when considering long term mineralization and/or dissolution behavior.

Fig. 12 shows the time- and space-averaged densities of H_2O, CO_2, and acetic acid or acetate species for systems composed of infinitely long supercritical CO_2 droplets surrounded by an aqueous phase containing CH_3COOH or $NaCH_3COO$ confined within muscovite slit pores of approximately 8 nm width at 333 K and 13.8 MPa. These simulations with trace amounts of acetate or acetic acid added to the CO_2/water/mineral system were used to investigate the potential effect of contamination with small organic molecules. While the observed contact angle was not significantly altered, these simulations demonstrate the influence of pH on species partitioning, with acetic acid molecules partitioning to the CO_2/water interface and acetate ions adsorbing to the mineral surface. Similar simulations using hexanoate displayed a greater surfactant effect and significantly increased wetting by the CO_2 phase, suggesting that small concentrations of secondary species or contaminants can significantly influence macroscopic wet-

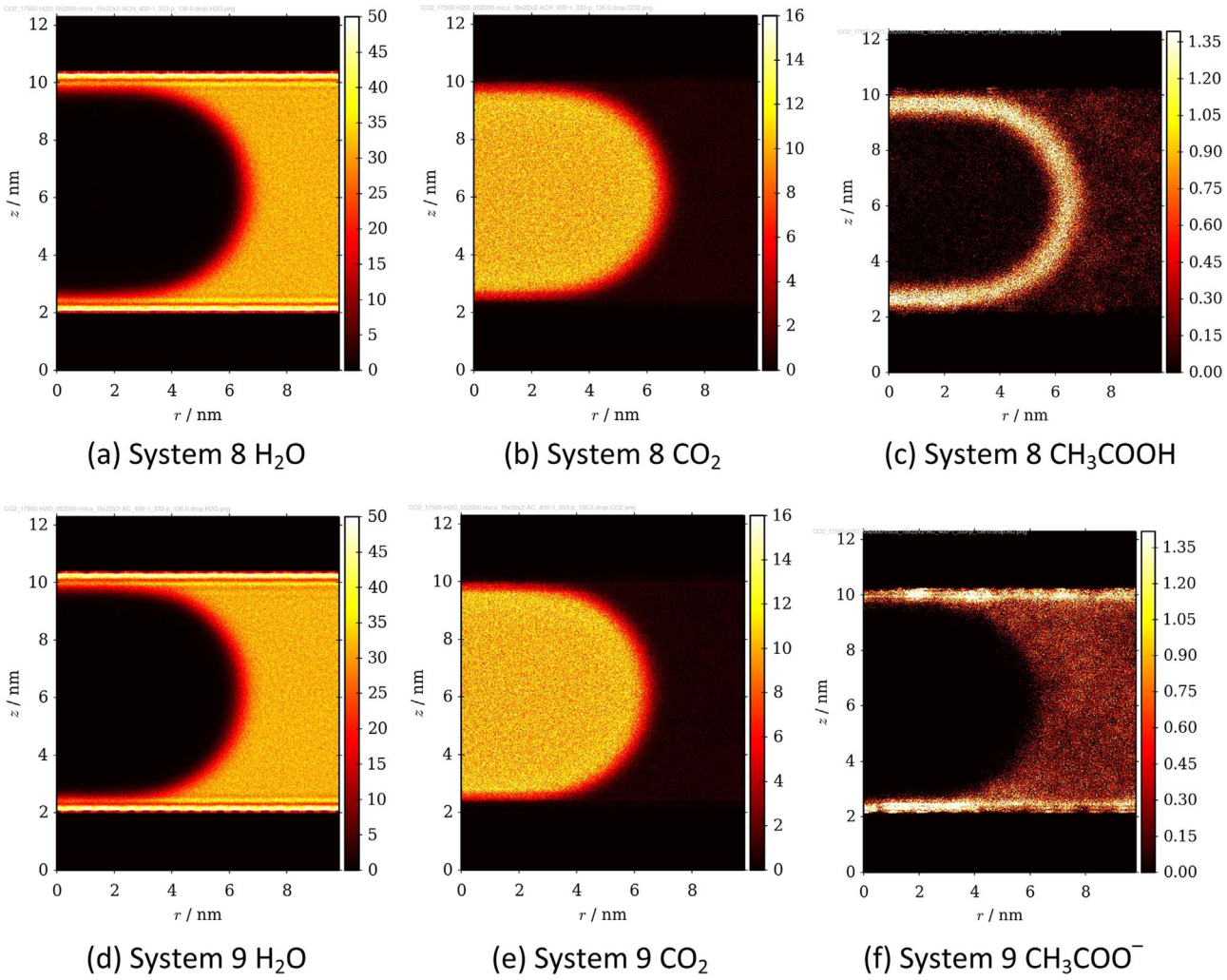

Fig. 12. Densities of H_2O, CO_2, and acetic acid or acetate averaged over the final 2 ns of simulation around and along the plane of (approximate) system symmetry passing through the long axis of the CO_2 droplet. Notation as in Fig. 10. (a) System 8H_2O. (b) System 8 CO_2. (c) System 8 CH_3COOH. (d) System 9H_2O. (e) System 9 CO_2. (f) System 9 CH_3COO^-.

ting behavior.

The strongly non-wetting character of CO_2 observed in these simulations differs significantly from the current experimental observations and prior work (Chiquet et al., 2007; Wan et al., 2014; Broseta et al., 2012; Arif et al., 2016). In addition to chemical and physical surface heterogeneity, which is not present in the simulation systems but likely inescapable in experiments, the presence of trace chemical species (for example, small organic molecules) offers another possible explanation for the difference in wetting behavior observed between experimental and these simulated systems. While we originally chose muscovite for ease of use, assuming it to be a relatively clean, flat, and easily characterized surface, the disagreement between contact angle results calculated for the ideal implementation of this assumption in simulation and experimental observations suggest our understanding of molecular scale details is far from complete.

5. Conclusions

Our experimental results indicate a small but measurable increase in water phase contact angle on fresh muscovite surfaces as a function of ionic strength, similar to that observed in soil (Leelamanie and Karube, 2013) and CO_2 (Farokhpoor et al., 2013) systems. This effect is attributable to an increase in liquid phase surface tension, or water-non wetting phase interfacial tension, with ionic strength (Jr et al., 1997; Leelamanie and Karube, 2013).

There has been recent and increasing attention on the influence of surface preparation, surface roughness, and potential surface contamination on wettability. While certain methods such as pre-treatment with oxidizing solutions may remove any potential organic contamination (Iglauer et al., 2014), such treatment may artificially decrease hydrophobicity (Saraji et al., 2014) and alter surface roughness so that perhaps the best alternative for contact angle studies is to examine mineral surface wettability under simulated subsurface conditions, including natural surface roughness and with in situ organic films, if present (Wan et al., 2014). One potential source of contamination that we can identify in our experimental results that has not been discussed in the literature could result from the interaction of the ethylene propylene o-rings with CO_2. Viton o-rings are known to exhibit an “explosive decompression”, or shredding due to absorption of CO_2 and subsequent decompression and change of CO_2 phase from sub critical or liquid to gas. Thus we use high durometer ethylene propylene o-rings to avoid any safety issues associated with potential viton (or other composition) o-ring failure. However, Bryan et al. (2013) (their Figure 21), in an FTIR study of water film interaction with CO_2, noted a small but measurable peak appearing in the IR spectra associated with organic contamination sourced from ethylene-propylene o-rings used in their study. It is possible that, despite rigor in surface preparation, interaction with o-rings, if used as sealant agents, could provide a source of additional contamination during high pressure contact angle measurements. The extent to which such contamination may have influenced our results is not known.

We used large-scale molecular dynamics simulations to investigate

wetting behavior in CO_2–brine systems on basal surfaces of the clay mineral muscovite. Clay minerals are present in many potential sites being considered for carbon sequestration, where the clay phases occur as coatings on sandstone grains and as the dominant mineral phase of shale caprocks. The muscovite surface was strongly wetting with respect to the aqueous phase and strongly non-wetting with respect to the CO_2 phase. A CO_2 droplet in the presence of water or brine did not interact directly with the muscovite surface, but instead interacted with a diffuse layer of H_2O molecules adsorbed to the mineral surface. Because nucleation and precipitation of carbonate minerals depend on the local distribution of CO_2, H_2O, and dissolved ion species, nanoscale surface interactions can influence mineralization of injected carbon. While mineral trapping is desired for secure sequestration of CO_2, precipitation and dissolution of minerals necessarily alter pore structure within the rock matrix, thereby influencing fluid transport. The long-term fate of CO_2 will ultimately be controlled by the mixing of the injected CO_2 with reservoir brine to achieve thermodynamic saturation. Reliably understanding, predicting, and controlling CO_2 sequestration will require accounting for complex, coupled mechanisms of reaction and transport over a wide range of time and length scales.

Acknowledgement

We thank Charles Bryan for providing the muscovite crystal from which our samples were taken, and chemical analysis and Yifeng Wang for useful discussions.

This material is based upon work supported as part of the Center for Frontiers of Subsurface Energy Security, an Energy Frontier Research Center funded by the U.S. Department of Energy, Office of Science, Office of Basic Energy Sciences under Award Number DE-SC0001114.

Sandia National Laboratories is a multi-mission laboratory managed and operated by Sandia Corporation, a wholly owned subsidiary of Lockheed Martin Corporation, for the U.S. Department of Energy's National Nuclear Security Administration under contract DE-AC04-94AL85000.

Appendix A. Supplementary material

Supplementary data associated with this article can be found in the online version at doi:10.1016/j.petrol.2016.10.010.

References

MetzB., 2005. I. P. on Climate Change. Working Group III., IPCC Special Report on Carbon Dioxide Capture and Storage, Cambridge University Press for the Intergovernmental Panel on Climate Change. URL ⟨http://books.google.com/books?Id=cJjCQgAACAAJ⟩.

Saadatpoor, E., Bryant, S., Sepehrnoori, K., 2010. New trapping mechanism in carbon sequestration. Transp. Porous Media 82 (1), 3–17. http://dx.doi.org/10.1007/s11242-009-9446-6.

Krevor, S.C.M., Pini, R., Li, B., Benson, S.M., 2011. Capillary heterogeneity trapping of CO_2 in a sandstone rock at reservoir conditions. Geophys. Res. Lett. 38 (15). http://dx.doi.org/10.1029/2011GL048239.

Wang, S.B., Edwards, I.M., Clarens, A.F., 2013. Wettability phenomena at the CO_2-Brine-mineral interface: implications for geologic carbon sequestration. Environ. Sci. Technol. 47, 234–241.

Parmigiani, A., Huber, C., Bachmann, O., Chopard, B., 2011. Pore-scale mass and reactant transport in multiphase porous media flows. J. Fluid Mech. 686, 40–76. http://dx.doi.org/10.1017/jfm.2011.268, (URL < GotoISI > //WOS:000297295900004)..

Iglauer, S., Pentland, C.H., Busch, A., 2015. CO_2 wettability of seal and reservoir rocks and the implications for carbon geo-sequestration. Water Resour. Res. 51 (1), 729–774. http://dx.doi.org/10.1002/2014WR015553.

Chiquet, P., Daridon, J.L., Broseta, D., Thibeau, S., 2007. CO_2/water interfacial tensions under pressure and temperature conditions of CO_2 geological storage. Energy Convers. Manag. 48, 736–744.

Chiquet, P., Broseta, D., Thibeau, S., 2007. Wettability alteration of caprock minerals by carbon dioxide. Geofluids 7 (2), 112–122. http://dx.doi.org/10.1111/j.1468-8123.2007.00168.x, (URL < GotoISI > //WOS:000245941200002).

Espinoza, D.N., Santamarina, J.C., 2010. Water-CO_2-mineral systems: interfacial tension, contact angle, and diffusion-implications to CO_2 geological storage. Water Resour. Res. 46, 10.

Bikkina, P.K., 2011. Contact angle measurements of CO_2-Water-quartz/calcite systems in the perspective of carbon sequestration. Int. J. Greenh. Gas. Control 5 (5), 1259–1271. http://dx.doi.org/10.1016/j.ijggc.2011.07.001, (URL < GotoISI > //WOS:000295300700016).

Kim, Y., Wan, J.M., Kneafsey, T.J., Tokunaga, T.K., 2012. Dewetting of silica surfaces upon reactions with supercritical CO_2 and brine: pore-scale studies in micromodels. Environ. Sci. Technol. 46, 4228–4235.

Saraji, S., Goual, L., Piri, M., Plancher, H., 2013. Wettability of supercritical carbon dioxide/water/quartz systems: simultaneous measurement of contact angle and interfacial tension at reservoir conditions. Langmuir 29 (23), 6856–6866. http://dx.doi.org/10.1021/la3050863, (URL < GotoISI > //WOS:000320485400011).

Heath, J.E., Dewers, T.A., McPherson, B., Nemer, M.B., Kotula, P.G., 2012. Porelining phases and capillary breakthrough pressure of mudstone caprocks: sealing efficiency of geologic CO_2 Storage sites. Int. J. Greenh. Gas. Control 11, 204–220. http://dx.doi.org/10.1016/j.ijggc.2012.08.001, (URL < GotoISI > //WOS:000313479200021).

Mahadevan, J., 2012. Comments on the paper titled “contact angle measurements of CO_2-Water-quartz/calcite systems in the perspective of carbon sequestration”: a case of contamination? Int. J. Greenh. Gas. Control 7, 261–262. http://dx.doi.org/10.1016/j.ijggc.2011.09.002, (URL < GotoISI > //WOS:000303290200027).

Wan, J., Kim, Y., Tokunaga, T.K., 2014. Contact angle measurement ambiguity in supercritical co2â¿waterâ¿mineral systems: mica as an example. Int. J. Greenh. Gas. Control 31, 128–137 . http://dx.doi.org/10.1016/j.ijggc.2014.09.029⟨http://www.sciencedirect.com/science/article/pii/⟩, (S1750583614002916).

Broseta, D., Tonnet, N., Shah, V., 2012. Are rocks still water-wet in the presence of dense CO_2 or h2S? Geofluids 12, 280–294.

Farokhpoor, R., Bjorkvik, B., Lindeberg, E., TorsÃter, O., 2013. Wettability behaviour of {CO_2} at storage conditions. Int. J. Greenh. Gas Control 12, 18–25 . http://dx.doi.org/10.1016/j.ijggc.2012.11.003⟨http://www.sciencedirect.com/science/article/pii/⟩, (S1750583612002551).

Iglauer, S., Salamah, A., Sarmadivaleh, M., Liu, K., Phan, C., 2014. Contamination of silica surfaces: impact on waterâ¿co2â¿quartz and glass contact angle measurements. Int. J. Greenh. Gas. Control 22, 325–328 . http://dx.doi.org/10.1016/j.ijggc.2014.01.006⟨http://www.sciencedirect.com/science/article/pii/⟩, (S1750583614000073).

Saraji, S., Piri, M., Goual, L., 2014. The effects of {SO2} contamination, brine salinity, pressure, and temperature on dynamic contact angles and interfacial tension of supercritical co2/brine/quartz systems. Int. J. Greenh. Gas Control 28, 147–155 . http://dx.doi.org/10.1016/j.ijggc.2014.06.024⟨http://www.sciencedirect.com/science/article/pii/⟩, (S1750583614001819).

Buckley, J.S., 2001. Effective wettability of minerals exposed to crude oil. Curr. Opin. Colloid Interface Sci. 6 (3), 191–196 . http://dx.doi.org/10.1016/S1359-0294(01)00083-8⟨http://www.sciencedirect.com/science/article/pii/⟩, (S1359029401000838).

Jr, F.T.B., Dawson, H.E., Christener, J.M., Honeyman, B.D., 1997. Influence of aqueous ph and ionic strength on the wettability of quartz in the presence of dense non-aqueous-phase liquids. Environ. Sci. Technol. 31 (3), 676–681. http://dx.doi.org/10.1021/es960217m.

Leelamanie, D., Karube, J., 2013. Soil-water contact angle as affected by the aqueous electrolyte concentration. Soil Sci. Plant Nutr. 59 (4), 501–508. http://dx.doi.org/10.1080/00380768.2013.809601.

Jung, J.-W., Wan, J., 2012. Supercritical CO_2 and ionic strength effects on wettability of silica surfaces: equilibrium contact angle measurements. Energy Fuels 26 (9), 6053–6059. http://dx.doi.org/10.1021/ef300913t.

Amirfazli, A., Neumann, A.W., 2004. Status of the three-phase line tension. Adv. Colloid Interface Sci. 110, 121–141.

Tadmor, R., 2008. Line energy, line tension and drop size. Surf. Sci. 602, L108–L111.

Brinkmann, M., Kierfeld, J., Lipowsky, R., 2005. Stability of liquid channels or filaments in the presence of line tension. J. Phys.-Condens. Matter 17, 2349–2364.

Plimpton, S.J., 1995. Fast parallel algorithms for short-range molecular dynamics. J. Comput. Phys. 117, 1–19.

PlimptonS.J.LAMMPS molecular dynamics simulator. URL ⟨http://lammps.sandia.gov⟩

Taherian, F., Marcon, V., van der Vegt, N.F.A., Leroy, F., 2013. What is the contact angle of water on graphene? Langmuir 29, 1457–1465.

Sergi, D., Scocchi, G., Ortona, A., 2012. Molecular dynamics simulations of the contact angle between water droplets and graphite surfaces. Fluid Phase Equilib. 332, 173–177.

Scocchi, G., Sergi, D., D'Angelo, C., Ortona, A., 2011. Wetting and contact-line effects for spherical and cylindrical droplets on graphene layers: a comparative molecular-dynamics investigation. Phys. Rev. E 84, 8.

Halverson, J.D., Maldarelli, C., Couzis, A., Koplik, J., 2009. Wetting of hydrophobic substrates by nanodroplets of aqueous trisiloxane and alkyl polyethoxylate surfactant solutions. Chem. Eng. Sci. 64, 4657–4667.

Wu, C.D., Kuo, L.M., Lin, S.J., Fang, T.H., Hsieh, S.F., 2012. Effects of temperature, size of water droplets, and surface roughness on nanowetting properties investigated using molecular dynamics simulation. Comput. Mater. Sci. 53, 25–30.

Holck, O., Bauer, J., Wittler, O., Michel, B., Wunderle, B., 2012. Comparative characterization of chip to epoxy interfaces by molecular modeling and contact angle determination. Microelectron. Reliab. 52, 1285–1290.

Iglauer, S., Mathew, M.S., Bresme, F., 2012. Molecular dynamics computations of brine-CO_2 interfacial tensions and brine-co2-quartz contact angles and their effects on structural and residual trapping mechanisms in carbon geosequestration. J. Colloid Interface Sci. 386, 405–414.

Solc, R., Gerzabek, M.H., Lischka, H., Tunega, D., 2011. Wettability of kaolinite (001) surfaces - molecular dynamic study. Geoderma 169, 47–54.

Tenney, C.M., Cygan, R.T., 2014. Molecular simulation of carbon dioxide, brine, and clay mineral interactions and determination of contact anglesEnviron. Sci. Technol. 48, 2035–2042 . http://dx.doi.org/10.1021/es404075k, (arXiv)⟨http://pubs.acs.org/doi/pdf/10.1021/es404075k⟩.

Nielsen, L.C., Bourg, I.C., Sposito, G., 2012. Predicting CO_2-Water interfacial tension under pressure and temperature conditions of geologic CO_2 Storage. Geochim. Cosmochim. Acta 81, 28–38.

Li, X., Ross, D.A., Trusler, J.P.M., Maitland, G.C., Boek, E.S., 2013. Molecular dynamics simulations of CO_2 and brine interfacial tension at high temperatures and pressures. J. Phys. Chem. B 117 (18), 5647–5652 . http://dx.doi.org/10.1021/jp309730m, (arXiv)⟨http://pubs.acs.org/doi/pdf/10.1021/jp309730m⟩.

Cygan, R.T., Liang, J.J., Kalinichev, A.G., 2004. Molecular models of hydroxide, oxyhydroxide, and clay phases and the development of a general force field. J. Phys. Chem. B 108 (4), 1255–1266.

Cygan, R.T., Romanov, V.N., Myshakin, E.M., 2012. Molecular simulation of carbon dioxide capture by montmorillonite using an accurate and flexible force field. J. Phys. Chem. C 116, 13079–13091.

Chaudhary, K., Guiltinan, E.J., Cardenas, M.B., Maisano, J.A., Ketcham, R.A., Bennett, P.C., 2015. Wettability measurement under high p-t conditions using x-ray imaging with application to the brine-supercritical CO_2 system. Geochem. Geophys. Geosyst. 16 (9), 2858–2864. http://dx.doi.org/10.1002/2015GC005936.

Ferreira, T., Rasband, WS. ImageJ User Guide — IJ 1.46, imagej.nih.gov/ij/docs/guide/, 2010—2012

Stalder, A.F., Melchior, T., Müller, M., Sage, D., Blu, T., Unser, M., 2010. Low-Bond Axisymmetric Drop Shape Analysis for Surface Tension and Contact Angle Measurements of Sessile Drops. Colloids and Surfaces A: Physicochemical and Engineering Aspects 364 (1–3), 72–81, July 20.

Gupta, V., Miller, J.D., 2010. Surface force measurements at the basal planes of ordered kaolinite particles. J. Colloid Interface Sci. 344 (2), 362–371. http://dx.doi.org/10.1016/j.jcis.2010.01.012, ⟨http://www.sciencedirect.com/science/article/pii/⟩(S0021979710000433).

Catti, M., Ferraris, G., Hull, S., Pavese, A., 1994. Powder neutron diffraction study of 2m 1 muscovite at room pressure and at 2 GPa. Eur. J. Mineral. 6 (2), 171–178 , (arXiv:http://eurjmin.geoscienceworld.org/content/6/2/171.full.pdf+html. URL) ⟨http://eurjmin.geoscienceworld.org/content/6/2/171.short⟩.

Wunsch, A., Navarre-Sitchler, A.K., McCray, J.E., 2013. Geochemical implications of brine leakage into freshwater aquifers. Groundwater 51 (6), 855–865. http://dx.doi.org/10.1111/gwat.12011.

Arif, M., Al-Yaseri, A.Z., Barifcani, A., Lebedev, M., Iglauer, S., 2016. Impact of pressure and temperature on CO_2–brine–mica contact angles and co2–brine interfacial tension: implications for carbon geosequestration. J. Colloid Interface Sci. 462, 208–215 . http://dx.doi.org/10.1016/j.jcis.2015.09.076, (URL)⟨http://www.sciencedirect.com/science/article/pii/S0021979715302460⟩.

BryanC., DewersT., HeathJ., WangY., MatteoE., MeseroleS., TallantD., 2013. Fundamental study of CO_2-H_2O-mineral interactions for carbon sequestration, with emphasis on the nature of the supercritical fluid-mineral interface, SAND Report SAND2013-8251, Sandia National Laboratories, Albuquerque, New Mexico.

Supporting Information for "Experimental and Simulation Study of Carbon Dioxide, Brine, and Muscovite Surface Interactions"

Craig M. Tenney,*,† Thomas Dewers,† Kuldeep Chaudhary,‡ Edward N. Matteo,† M. Bayani Cardenas,‡ and Randall T. Cygan†

†*Sandia National Laboratories, Albuquerque, New Mexico, United States*

‡*University of Texas, Austin, Texas, United States*

E-mail: cmtenne@sandia.gov

This Supporting Information document contains the following sections:

- Simulation Details: details describing the setup and analysis of the systems studied in this work
- Force Fields: parameters used for the calculation of energies and forces in the molecular simulations described in this work
- Example LAMMPS Scripts: examples of the LAMMPS scripts used to set up and conduct the molecular simulations described in this work

Simulation Details

Figure S1 shows the structure for a muscovite unit cell. Each silicon (or substituted aluminum) atom in the tetrahedral sheets is connected to three other silicon (or substituted

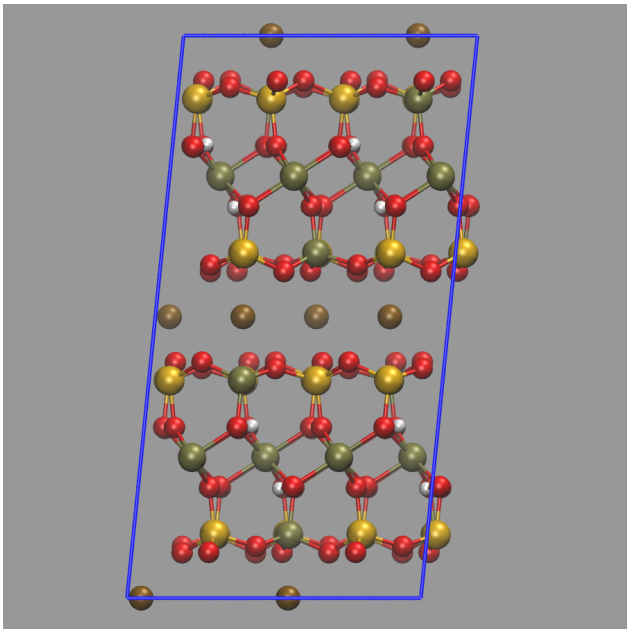

Figure S1: Crystal structure of a two-layer muscovite unit cell. Oxygen atoms are depicted by red vertices, hydrogen by white, aluminum by tan, silicon by orange, and interlayer potassium ions by brown.

aluminum) atoms by bridging oxygens forming the siloxane surface. This tetrahedral arrangement gives rise to hexagonal cavities on the surface. Each aluminum in the octahedral sheet is coordinated by two oxygens of the siloxane sheet and shares four hydroxyls with neighboring aluminum atoms. This layered structure extends to edges of the crystal where exposed dangling silicon and aluminum atoms are terminated by hydroxyls at low pH conditions.

The mineral phase used in each simulation was composed of four layers of muscovite (140,448 atoms). Initial atom positions within the muscovite slab were assigned by replicating a unit cell derived from nuetron diffraction data[1]. The muscovite slab measures approximately 198 Å and 199 Å in the transverse (x and y) directions and 40 Å thick. Simulation cell boundaries in the x and y directions are periodic and sized to match the dimensions of the muscovite slab, resulting in an infinite slab with no edges. Simulation cell boundaries in the z direction are periodic and sized to contain the muscovite slab and fluid adjacent to the slab, resulting in an infinite series of muscovite slabs separated by fluid layers.

The thickness of the fluid region varies, depending on the pressure applied and amount of fluid present.

Muscovite was modeled using the fully-flexible ClayFF force field[2]. ClayFF uses an empirically derived set of interaction parameters to accurately describe the potential energy between atoms in the clay structure. ClayFF has been used extensively to successfully simulate many oxide, hydroxide, and hydrated systems including bulk and interfacial structures[2–6]. Metal-oxygen interactions are described by a 12-6 Lennard-Jones (LJ) term and a Coulombic function with partial charges derived by quantum chemistry methods. The only explicit bonded interactions are those within hydroxyl groups (bond stretch), which are based on the SPC water model[7]. To prevent unphysical oscillation of the muscovite slab, potassium ions atoms furthest from the fluid interfaces (i.e. the interlayer with two muscovite layers above and below) were held fixed during the simulations.

The water and dissolved ion models used in this work were chosen for consistency with ClayFF. ClayFF uses the three-point simple point charge (SPC) water model[7], combined with harmonic bond stretching and angle bending terms based on the intramolecular parameters from Teleman et al.[8]. Interatomic potentials for water that incorporate bond flexibility have demonstrated improved predictions of properties across a wide range of state points compared to rigid models[9,10]. Having one LJ center at the oxygen atom and partial charges centered directly on each of the three atoms, the SPC water model is relatively simple and has been used to study properties of bulk water and aqueous systems[7,8,11,12]. ClayFF uses force field parameters from the literature to represent the aqueous species Ca^{2+}[13], Na^{+}[14], and Cl^{-}[14].

Supercritical CO_2 was also modeled using a fully flexible force field[15]. In this three-point force field, each atom is represented by a LJ center and partial charge to account for non-bonded energies. Bond stretch and angle bend terms account for intramolecular energies. The force field uses the LJ parameters of Zhu et al.[16], which were refined from the original model of Harris and Yung[17]. The harmonic intramolecular bond stretch and angle bend

parameters were optimized to reproduce the vibrational spectra of CO_2[15].

All simulations were conducted using the open-source LAMMPS (version: 25 Jul 2012) molecular dynamics software package[18,19]. Temperature and pressure were maintained via a Nose-Hoover thermostat and barostat implemented in the standard LAMMPS code. Initial system configurations were all constructed using Packmol[20], an open-source simulation setup tool.

Total simulation times of 10 ns to 25 ns were used to allow droplets to equilibrate with the surrounding bulk fluid before collecting data for analysis. A typical system in this study contained approximately ∼400k atoms. System trajectory snapshots were recorded every 10 ps. These trajectories were post-processed to visualize molecular configurations and to calculate average local densities of CO_2, water, and brine species. A system was assumed to be sufficiently equilibrated when the number and distribution of molecules within the droplet stopped changing with time.

Force Fields

```
FORCEFIELD CO2-Cygan


! SETTING:
!! vdw_scaling: van der Waals interaction scaling coeffs for bonded atoms
!!! scale_12 (float): scale factor for 1-2 interactions
!!! scale_13 (float): scale factor for 1-3 interactions
!!! scale_14 (float): scale factor for 1-4 interactions
!! vdw_cutoff:
!!! style (str, ('cut', 'shift', 'correct')): cutoff style
!!! cutoff (float, angstrom): cutoff distance
!! vdw_switch:
```

```
!!! style (str, ('charmm',)): switch style
!!! switch_inner (float, angstrom): inner switch distance
!!! switch_outer (float, angstrom): outer switch distance
!! vdw_mix:
!!! style (str, ('LJ',)): interaction style
!!! mixrule (str, ('LB', 'geometric')): mixing rule
!! charge_scaling: charge interaction scaling coefficients for bonded atoms
!!! scale_12 (float): scale factor for 1-2 interactions
!!! scale_13 (float): scale factor for 1-3 interactions
!!! scale_14 (float): scale factor for 1-4 interactions
!! charge_cutoff:
!!! style (str, ('cut', 'ewald')): cutoff style
!!! cutoff (float, angstrom): cutoff distance
# typically for use with CLAYFF
SETTING  ! 5
  vdw_scaling 0.0000 0.0000 1.0000
  vdw_cutoff cut 12.0 # ?
  vdw_mix LJ LB
  charge_scaling 0.0000 0.0000 1.0000
  charge_cutoff ewald 12.0 # ?

! ATOM:
!! name (str): atom name (required)
!! mass (float, amu): atomic mass
!! element (str): element symbol
!! epsilon (float, Ken): LJ well depth
!! sigma (float, angstrom): LJ zero-energy distance (rmin/2**(1/6))
```

```
!! charge (float, e): partial atomic charge
ATOM name charge epsilon sigma element mass ! 2
   c       0.6512       28.144 2.800  C   12.011 # CO2 carbon ! 1
   o      -0.3256       80.378 3.028  O   15.999 # CO2 oxygen ! 2

! BOND:
!! harmonic: K * (R - R0)**2
!!! K (float, Ken/angstrom^2): force constant
!!! R0 (float, angstrom): equilibrium bond length
!! fixed: R = R0
!!! R0 (float, angstrom): equilibrium bond length
BOND  ! 1
   c    o harmonic      1015458  1.162  ! 1    1.160

! ANGLE:
!! harmonic: K * (A - A0)**2
!!! K (float, Ken/radian^2): force constant
!!! A0 (float, degrees): equilibrium angle
!! fixed: A = A0
!!! A0 (float, degrees): equilibrium angle
ANGLE  ! 1
   o    c    o harmonic        54351  180.00  ! 1  180.000

MOLECULE CO2

! ATOM:
!! name (str): atom name (required)
```

```
!! type (str): atom type name
!! charge (float, e): partial atomic charge
!! x (float, angstrom): atom coordinate
!! y (float, angstrom): atom coordinate
!! z (float, angstrom): atom coordinate
ATOM name type x y z ! 3
   C    c    0.0000    0.0000    0.0000  ! 1
  O1    o   -1.1600    0.0000    0.0000  ! 2
  O2    o    1.1600    0.0000    0.0000  ! 3

! BOND:
BOND  ! 2
   C   O1   ! 1    1.160
   C   O2   ! 2    1.160

! ANGLE:
ANGLE  ! 1
  O1    C   O2   ! 1  180.000

# converted from OpenMD CLAYFF.frc
FORCEFIELD H2O-clayff

! SETTING:
!! vdw_scaling: van der Waals interaction scaling coeffs for bonded atoms
!!! scale_12 (float): scale factor for 1-2 interactions
!!! scale_13 (float): scale factor for 1-3 interactions
!!! scale_14 (float): scale factor for 1-4 interactions
```

```
!! vdw_cutoff:
!!! style (str, ('cut', 'shift', 'correct')): cutoff style
!!! cutoff (float, angstrom): cutoff distance
!! vdw_switch:
!!! style (str, ('charmm',)): switch style
!!! switch_inner (float, angstrom): inner switch distance
!!! switch_outer (float, angstrom): outer switch distance
!! vdw_mix:
!!! style (str, ('LJ',)): interaction style
!!! mixrule (str, ('LB', 'geometric')): mixing rule
!! charge_scaling: charge interaction scaling coefficients for bonded atoms
!!! scale_12 (float): scale factor for 1-2 interactions
!!! scale_13 (float): scale factor for 1-3 interactions
!!! scale_14 (float): scale factor for 1-4 interactions
!! charge_cutoff:
!!! style (str, ('cut', 'ewald')): cutoff style
!!! cutoff (float, angstrom): cutoff distance
SETTING  ! 5
  vdw_scaling 0.0000 0.0000 1.0000
  vdw_cutoff cut 12.0 # ?
  vdw_mix LJ LB
  charge_scaling 0.0000 0.0000 1.0000
  charge_cutoff ewald 12.0 # ?

! ATOM:
!! name (str): atom name (required)
!! mass (float, amu): atomic mass
```

```
!! element (str): element symbol
!! epsilon (float, Ken): LJ well depth
!! sigma (float, angstrom): LJ zero-energy distance (rmin/2**(1/6))
!! charge (float, e): partial atomic charge
ATOM name charge epsilon sigma element mass ! 2
  h*         0.41            0 0.000  H    1.008 # water hydrogen ! 1
  o*        -0.82     78.25256 3.166  O   15.999 # water oxygen ! 2

! BOND:
!! harmonic: K * (R - R0)**2
!!! K (float, Ken/angstrom^2): force constant
!!! R0 (float, angstrom): equilibrium bond length
!! fixed: R = R0
!!! R0 (float, angstrom): equilibrium bond length
BOND  ! 1
  h*   o* harmonic       279038  1.000  ! 1    0.969

! ANGLE:
!! harmonic: K * (A - A0)**2
!!! K (float, Ken/radian^2): force constant
!!! A0 (float, degrees): equilibrium angle
!! fixed: A = A0
!!! A0 (float, degrees): equilibrium angle
ANGLE  ! 1
  h*   o*   h* harmonic        23048  109.47  ! 1  103.996

MOLECULE H2O
```

```
! ATOM:
!! name (str): atom name (required)
!! type (str): atom type name
!! charge (float, e): partial atomic charge
!! x (float, angstrom): atom coordinate
!! y (float, angstrom): atom coordinate
!! z (float, angstrom): atom coordinate
ATOM name type x y z ! 3
   O   o*    0.0000   -0.0643    0.0000  ! 1
  H1   h*   -0.7633    0.5321    0.0000  ! 2
  H2   h*    0.7633    0.5321    0.0000  ! 3

! BOND:
BOND  ! 2
  H1    O   ! 1    0.969
  H2    O   ! 2    0.969

! ANGLE:
ANGLE  ! 1
  H1    O   H2   ! 1  103.996

# converted from OpenMD CLAYFF.frc
# This is the forcefield file for the Clay Force Field (CLAYFF)
# Details can be found in the following article:
# "Molecular Models of Hydroxide, Oxyhydroxid, and Clay Phases and
# the Development of a General Force Field" by Randall T. Cygan,
```

```
# Jian-Jie Liang, and Andrey G. Kalinichev, J. Phys. Chem. B 108,
# pp. 1255-1266 (2004).
FORCEFIELD clayff

! SETTING:
!! vdw_scaling: van der Waals interaction scaling coeffs for bonded atoms
!!! scale_12 (float): scale factor for 1-2 interactions
!!! scale_13 (float): scale factor for 1-3 interactions
!!! scale_14 (float): scale factor for 1-4 interactions
!! vdw_cutoff:
!!! style (str, ('cut', 'shift', 'correct')): cutoff style
!!! cutoff (float, angstrom): cutoff distance
!! vdw_switch:
!!! style (str, ('charmm',)): switch style
!!! switch_inner (float, angstrom): inner switch distance
!!! switch_outer (float, angstrom): outer switch distance
!! vdw_mix:
!!! style (str, ('LJ',)): interaction style
!!! mixrule (str, ('LB', 'geometric')): mixing rule
!! charge_scaling: charge interaction scaling coefficients for bonded atoms
!!! scale_12 (float): scale factor for 1-2 interactions
!!! scale_13 (float): scale factor for 1-3 interactions
!!! scale_14 (float): scale factor for 1-4 interactions
!! charge_cutoff:
!!! style (str, ('cut', 'ewald')): cutoff style
!!! cutoff (float, angstrom): cutoff distance
SETTING  ! 5
```

```
  vdw_scaling 0.0000 0.0000 1.0000
  vdw_cutoff cut 12.0 # ?
  vdw_mix LJ LB
  charge_scaling 0.0000 0.0000 1.0000
  charge_cutoff ewald 12.0 # ?

! ATOM:
!! name (str): atom name (required)
!! mass (float, amu): atomic mass
!! element (str): element symbol
!! epsilon (float, Ken): LJ well depth
!! sigma (float, angstrom): LJ zero-energy distance (rmin/2**(1/6))
!! charge (float, e): partial atomic charge
ATOM name charge epsilon sigma element mass ! 24
  h*         0.41            0 0.000  H    1.008 # water hydrogen ! 1
  ho        0.425            0 0.000  H    1.008 # hydroxyl hydrogen ! 2
  o*        -0.82     78.25256 3.166  O   15.999 # water oxygen ! 3
  oh        -0.95     78.25256 3.166  O   15.999 # hydroxyl oxygen ! 4
  ob        -1.05     78.25256 3.166  O   15.999 # bridging oxygen ! 5
obos      -1.1808     78.25256 3.166  O   15.999 # bridging oxygen with octahedral subst
obts     -1.16875     78.25256 3.166  O   15.999 # bridging oxygen with tetrahedral subs
obss      -1.2996     78.25256 3.166  O   15.999 # bridging oxygen with double substitut
 ohs      -1.0808     78.25256 3.166  O   15.999 # hydroxyl oxygen with substitution ! 9
  st          2.1 0.0009267943 3.302 Si   28.085 # tetrahedral silicon ! 10
  ao        1.575 0.0006696284 4.271 Al   26.982 # octahedral aluminum ! 11
  at        1.575 0.0009267943 3.302 Al   26.982 # tetrahedral aluminum ! 12
 mgo         1.36 0.0004547008 5.264 Mg   24.305 # octahedral magnesium ! 13
```

```
 mgh         1.05 0.0004547008 5.264 Mg   24.305 # hydroxide magnesium ! 14
 cao         1.36  0.002532785 5.567 Ca   40.078 # octahedral calcium ! 15
 cah         1.05  0.002532785 5.562 Ca   40.078 # hydroxide calcium ! 16
 feo        1.575  0.004547008 4.906 Fe   55.845 # octahedral iron ! 17
 lio        0.525  0.004547008 4.210 Li    6.941 # octahedral lithium ! 18
  Na            1      65.5126 2.350 Na   22.990 # aqueous sodium ion ! 19
   K            1     50.35557 3.334  K   39.098 # aqueous potassium ion ! 20
  Cs            1     50.35557 3.831 Cs  132.905 # aqueous cesium ion ! 21
  Ca            2     50.35557 2.872 Ca   40.078 # aqueous calcium ion ! 22
  Ba            2     23.66711 3.817 Ba  137.327 # aqueous barium ion ! 23
  Cl           -1     50.40593 4.400 Cl   35.453 # aqueous chloride ion ! 24

! BOND:
!! harmonic: K * (R - R0)**2
!!! K (float, Ken/angstrom^2): force constant
!!! R0 (float, angstrom): equilibrium bond length
!! fixed: R = R0
!!! R0 (float, angstrom): equilibrium bond length
BOND  ! 3
  h*   o* harmonic       279038  1.000  ! 1
  ho   oh harmonic       279038  1.000  ! 2    0.947
  ho  ohs harmonic       279038  1.000  ! 3

# ANGLE
# h*  o*  h* harmonic 23048 109.47
# ao  oh  ho harmonic 15107 109.47
# ao  ohs ho harmonic 15107 109.47
```

```
# at  oh  ho harmonic 15107 109.47
# at  ohs ho harmonic 15107 109.47
# mgh oh  ho harmonic 15107 109.47
# mgh ohs ho harmonic 15107 109.47
# cah oh  ho harmonic 15107 109.47
# cah ohs ho harmonic 15107 109.47
# feo oh  ho harmonic 15107 109.47
# feo ohs ho harmonic 15107 109.47
# lio oh  ho harmonic 15107 109.47
# lio ohs ho harmonic 15107 109.47
MOLECULE mica

! SETTING:
!! unitcell: unit cell dimensions (for crystalline materials only)
!!! a (float, angstrom): unit cell edge length
!!! b (float, angstrom): unit cell edge length
!!! c (float, angstrom): unit cell edge length
!!! alpha (float, degree): unit cell angle
!!! beta (float, degree): unit cell angle
!!! gamma (float, degree): unit cell angle
!!! space_group (str, P1): space group
SETTING  ! 1
  unitcell 10.422  9.040 20.021  90.00  95.76  90.00 P1

! ATOM:
!! name (str): atom name (required)
!! type (str): atom type name
```

```
!! charge (float, e): partial atomic charge
!! x (float, angstrom): atom coordinate
!! y (float, angstrom): atom coordinate
!! z (float, angstrom): atom coordinate
ATOM name x y z type ! 168
Si1a    2.1394    8.3773    7.7189   st  ! 1
Si2a    2.0935    2.3377    7.6990   st  ! 2
Al1a    1.2990    0.7539    4.9600   ao  ! 3
 O1a    1.8933    0.8443    8.3404   ob  ! 4
 O2a    0.9607    7.3711    8.1273 obts  ! 5
 O3a    0.9491    3.3113    8.3564   ob  ! 6
 O4a    2.3089    8.5147    6.0496   ob  ! 7
 O5a    1.9278    2.2645    6.0456   ob  ! 8
 O6a    2.2617    5.0849    6.0058   oh  ! 9
 H1a    1.7855    5.8985    6.0934   ho  ! 10
Si3a    4.7448    3.8573    7.7189   st  ! 11
Al2a    4.6989    6.8577    7.6990   at  ! 12
Al3a    3.9044    5.2739    4.9600   ao  ! 13
 O7a    4.4987    5.3643    8.3404 obts  ! 14
 O8a    3.5661    2.8512    8.1273 obts  ! 15
 O9a    3.5545    7.8313    8.3564   ob  ! 16
O10a    4.9143    3.9947    6.0496   ob  ! 17
O11a    4.5332    6.7844    6.0456   ob  ! 18
O12a    4.8671    0.5650    6.0058   oh  ! 19
 H2a    4.3909    1.3786    6.0934   ho  ! 20
Al4a    2.0667    8.3773   12.2009   at  ! 21
Si4a    2.1126    2.3377   12.2208   st  ! 22
```

```
Al5a    2.9072    0.7539   14.9598    ao  ! 23
O13a    2.3128    0.8443   11.5794  obts  ! 24
O14a    3.2454    7.3711   11.7925  obts  ! 25
O15a    3.2570    3.3113   11.5635    ob  ! 26
O16a    1.8973    8.5147   13.8702  obts  ! 27
O17a    2.2783    2.2645   13.8742    ob  ! 28
O18a    1.9444    5.0849   13.9140    oh  ! 29
 H3a    2.4207    5.8985   13.8264    ho  ! 30
Si5a   -0.5387    3.8573   12.2009    st  ! 31
Si6a   -0.4928    6.8577   12.2208    st  ! 32
Al6a    0.3018    5.2739   14.9598    ao  ! 33
O19a   -0.2926    5.3643   11.5794    ob  ! 34
O20a    0.6400    2.8512   11.7925    ob  ! 35
O21a    0.6516    7.8313   11.5635  obts  ! 36
O22a   -0.7081    3.9947   13.8702    ob  ! 37
O23a   -0.3271    6.7844   13.8742    ob  ! 38
O24a   -0.6610    0.5650   13.9140    oh  ! 39
 H4a   -0.1847    1.3786   13.8264    ho  ! 40
Al7a    3.0714    0.6626    2.2409    at  ! 41
Si7a    3.1173    6.7022    2.2609    st  ! 42
Al8a    3.9118    8.2860    4.9998    ao  ! 43
O25a    3.3175    8.1956    1.6194  obts  ! 44
O26a    4.2501    1.6688    1.8326  obts  ! 45
O27a    4.2617    5.7286    1.6035    ob  ! 46
O28a    2.9019    0.5252    3.9102  obts  ! 47
O29a    3.2830    6.7754    3.9142    ob  ! 48
O30a    2.9491    3.9550    3.9540    oh  ! 49
```

```
 H5a    3.4253    3.1414    3.8664   ho  ! 50
Si8a    0.4660    5.1826    2.2409   st  ! 51
Si9a    0.5119    2.1822    2.2609   st  ! 52
Al9a    1.3064    3.7660    4.9998   ao  ! 53
O31a    0.7121    3.6756    1.6194   ob  ! 54
O32a    1.6447    6.1887    1.8326   ob  ! 55
O33a    1.6563    1.2086    1.6035 obts  ! 56
O34a    0.2965    5.0452    3.9102   ob  ! 57
O35a    0.6776    2.2555    3.9142   ob  ! 58
O36a    0.3437    8.4749    3.9540   oh  ! 59
 H6a    0.8199    7.6613    3.8664   ho  ! 60
Si10a    1.1348    0.6626   17.6789   st  ! 61
Si11a    1.0888    6.7022   17.6590   st  ! 62
Al10a    0.2943    8.2860   14.9200   ao  ! 63
O37a    0.8887    8.1956   18.3004   ob  ! 64
O38a   -0.0439    1.6688   18.0872   ob  ! 65
O39a   -0.0556    5.7286   18.3163 obts  ! 66
O40a    1.3042    0.5252   16.0096   ob  ! 67
O41a    0.9232    6.7754   16.0056   ob  ! 68
O42a    1.2570    3.9550   15.9658   oh  ! 69
 H7a    0.7808    3.1414   16.0534   ho  ! 70
Al11a    3.7402    5.1826   17.6789   at  ! 71
Si12a    3.6942    2.1822   17.6590   st  ! 72
Al12a    2.8997    3.7660   14.9200   ao  ! 73
O43a    3.4941    3.6756   18.3004 obts  ! 74
O44a    2.5615    6.1887   18.0872   ob  ! 75
O45a    2.5498    1.2086   18.3163 obts  ! 76
```

```
O46a    3.9096    5.0452   16.0096 obts  ! 77
O47a    3.5286    2.2555   16.0056 obts  ! 78
O48a    3.8624    8.4749   15.9658   oh  ! 79
 H8a    3.3862    7.6613   16.0534   ho  ! 80
 K1a   -0.5023    0.8579    9.9599    K  ! 81
 K2a    2.1031    5.3778    9.9599    K  ! 82
 K3a   -1.5070    8.1820   19.9199    K  ! 83
 K4a    3.1070    3.6620    0.0000    K  ! 84
Si1b    7.3504    8.3773    7.7189   st  ! 85
Si2b    7.3045    2.3377    7.6990   st  ! 86
Al1b    6.5100    0.7539    4.9600   ao  ! 87
 O1b    7.1043    0.8443    8.3404   ob  ! 88
 O2b    6.1717    7.3711    8.1273   ob  ! 89
 O3b    6.1601    3.3113    8.3564 obts  ! 90
 O4b    7.5199    8.5147    6.0496   ob  ! 91
 O5b    7.1388    2.2645    6.0456   ob  ! 92
 O6b    7.4727    5.0849    6.0058   oh  ! 93
 H1b    6.9965    5.8985    6.0934   ho  ! 94
Al2b    9.9558    3.8573    7.7189   at  ! 95
Si3b    9.9099    6.8577    7.6990   st  ! 96
Al3b    9.1154    5.2739    4.9600   ao  ! 97
 O7b    9.7097    5.3643    8.3404 obts  ! 98
 O8b    8.7771    2.8512    8.1273   ob  ! 99
 O9b    8.7655    7.8313    8.3564 obts  ! 100
O10b   10.1253    3.9947    6.0496 obts  ! 101
O11b    9.7442    6.7844    6.0456 obts  ! 102
O12b   10.0781    0.5650    6.0058   oh  ! 103
```

```
 H2b    9.6019    1.3786    6.0934   ho  ! 104
Si4b    7.2777    8.3773   12.2009   st  ! 105
Al4b    7.3236    2.3377   12.2208   at  ! 106
Al5b    8.1182    0.7539   14.9598   ao  ! 107
O13b    7.5238    0.8443   11.5794 obts  ! 108
O14b    8.4564    7.3711   11.7925   ob  ! 109
O15b    8.4680    3.3113   11.5635 obts  ! 110
O16b    7.1083    8.5147   13.8702   ob  ! 111
O17b    7.4893    2.2645   13.8742 obts  ! 112
O18b    7.1554    5.0849   13.9140   oh  ! 113
 H3b    7.6317    5.8985   13.8264   ho  ! 114
Si5b    4.6723    3.8573   12.2009   st  ! 115
Si6b    4.7182    6.8577   12.2208   st  ! 116
Al6b    5.5128    5.2739   14.9598   ao  ! 117
O19b    4.9184    5.3643   11.5794   ob  ! 118
O20b    5.8510    2.8512   11.7925 obts  ! 119
O21b    5.8626    7.8313   11.5635   ob  ! 120
O22b    4.5029    3.9947   13.8702   ob  ! 121
O23b    4.8839    6.7844   13.8742   ob  ! 122
O24b    4.5500    0.5650   13.9140   oh  ! 123
 H4b    5.0263    1.3786   13.8264   ho  ! 124
Si7b    8.2824    0.6626    2.2409   st  ! 125
Al7b    8.3283    6.7022    2.2609   at  ! 126
Al8b    9.1228    8.2860    4.9998   ao  ! 127
O25b    8.5285    8.1956    1.6194 obts  ! 128
O26b    9.4611    1.6688    1.8326   ob  ! 129
O27b    9.4727    5.7286    1.6035 obts  ! 130
```

```
O28b    8.1129    0.5252    3.9102   ob  ! 131
O29b    8.4940    6.7754    3.9142 obts  ! 132
O30b    8.1601    3.9550    3.9540   oh  ! 133
 H5b    8.6363    3.1414    3.8664   ho  ! 134
Si8b    5.6770    5.1826    2.2409   st  ! 135
Si9b    5.7229    2.1822    2.2609   st  ! 136
Al9b    6.5174    3.7660    4.9998   ao  ! 137
O31b    5.9231    3.6756    1.6194   ob  ! 138
O32b    6.8557    6.1887    1.8326 obts  ! 139
O33b    6.8673    1.2086    1.6035   ob  ! 140
O34b    5.5075    5.0452    3.9102   ob  ! 141
O35b    5.8886    2.2555    3.9142   ob  ! 142
O36b    5.5547    8.4749    3.9540   oh  ! 143
 H6b    6.0309    7.6613    3.8664   ho  ! 144
Si10b    6.3458    0.6626   17.6789   st  ! 145
Si11b    6.2998    6.7022   17.6590   st  ! 146
Al10b    5.5053    8.2860   14.9200   ao  ! 147
O37b    6.0997    8.1956   18.3004   ob  ! 148
O38b    5.1671    1.6688   18.0872 obts  ! 149
O39b    5.1554    5.7286   18.3163   ob  ! 150
O40b    6.5152    0.5252   16.0096   ob  ! 151
O41b    6.1342    6.7754   16.0056   ob  ! 152
O42b    6.4680    3.9550   15.9658   oh  ! 153
 H7b    5.9918    3.1414   16.0534   ho  ! 154
Si12b    8.9512    5.1826   17.6789   st  ! 155
Al11b    8.9052    2.1822   17.6590   at  ! 156
Al12b    8.1107    3.7660   14.9200   ao  ! 157
```

```
O43b    8.7051    3.6756   18.3004 obts  ! 158
O44b    7.7725    6.1887   18.0872 obts  ! 159
O45b    7.7608    1.2086   18.3163   ob  ! 160
O46b    9.1206    5.0452   16.0096   ob  ! 161
O47b    8.7396    2.2555   16.0056   ob  ! 162
O48b    9.0734    8.4749   15.9658   oh  ! 163
 H8b    8.5972    7.6613   16.0534   ho  ! 164
 K1b    4.7087    0.8579    9.9599    K  ! 165
 K2b    7.3141    5.3778    9.9599    K  ! 166
 K3b    3.7040    8.1820   19.9199    K  ! 167
 K4b    8.3180    3.6620    0.0000    K  ! 168

! BOND:
BOND  ! 16
 H1a  O6a   ! 1    0.947
 H2a O12a   ! 2    0.947
 H3a O18a   ! 3    0.947
 H4a O24a   ! 4    0.947
 H5a O30a   ! 5    0.947
 H6a O36a   ! 6    0.947
 H7a O42a   ! 7    0.947
 H8a O48a   ! 8    0.947
 H1b  O6b   ! 9    0.947
 H2b O12b   ! 10    0.947
 H3b O18b   ! 11    0.947
 H4b O24b   ! 12    0.947
 H5b O30b   ! 13    0.947
```

```
 H6b O36b   ! 14    0.947
 H7b O42b   ! 15    0.947
 H8b O48b   ! 16    0.947

# for use with CLAYFF
MOLECULE Na

! ATOM:
!! name (str): atom name (required)
!! type (str): atom type name
!! charge (float, e): partial atomic charge
!! x (float, angstrom): atom coordinate
!! y (float, angstrom): atom coordinate
!! z (float, angstrom): atom coordinate
ATOM name type x y z ! 1
  Na   Na    0.0000    0.0000    0.0000  ! 1

# for use with CLAYFF
MOLECULE Ca

! ATOM:
!! name (str): atom name (required)
!! type (str): atom type name
!! charge (float, e): partial atomic charge
!! x (float, angstrom): atom coordinate
!! y (float, angstrom): atom coordinate
!! z (float, angstrom): atom coordinate
```

```
ATOM name type x y z ! 1
  Ca   Ca    0.0000    0.0000    0.0000  ! 1

# for use with CLAYFF
MOLECULE Cl

! ATOM:
!! name (str): atom name (required)
!! type (str): atom type name
!! charge (float, e): partial atomic charge
!! x (float, angstrom): atom coordinate
!! y (float, angstrom): atom coordinate
!! z (float, angstrom): atom coordinate
ATOM name type x y z ! 1
  Cl   Cl    0.0000    0.0000    0.0000  ! 1
```

Example LAMMPS Scripts

System Setup

```
# read lammps data file, write a restart file

 # these variables must be set from the command line:
variable        outname index init
variable        infile index init.data

 # optional
# initial temperature (do nothing if < 0)
```

```
variable        beg_temp index -1

 # these variables have generally conservative defaults:
 # kspace: 1 = pppm, 2 = ewald, 3 = ewald/n, other = off
variable        kspace index 1
 # restart != 0: write_restart at end of script
variable        restart index 1

# ___end command line variable section___

# set up simulation
# the following information is saved to restart files
units           real
atom_style      full
boundary        p p p
pair_style      lj/cut/coul/long 12
pair_modify     tail yes
pair_modify mix arithmetic
special_bonds lj 0.000000 0.000000 1.000000
special_bonds coul 0.000000 0.000000 1.000000
bond_style harmonic
angle_style harmonic



read_data       ${infile}
# end information that is saved to restart files
```

```
if "${kspace} == 1" then "kspace_style pppm 0.0001"
if "${kspace} == 2" then "kspace_style ewald 0.0001"
if "${kspace} == 3" then "kspace_style ewald/n 0.0001"

if "${beg_temp} >= 0" then &
"velocity all create ${beg_temp} 24601 mom yes rot yes dist gaussian"

if "${restart} != 0" then &
"write_restart   ${outname}.restart.*"
```

NPT Simulation

```
# Choose ensemble/integrator by (un)commenting appropriate line(s).

 # naming conventions
variable outname index t_333-p_136.1
variable infile index init.restart.*
variable numsteps index 8000000

 # thermostat settings (if applicable)
variable beg_temp index 333
variable        end_temp index ${beg_temp}
 # barostat settings (if applicable)
variable beg_press index 136.09
variable        end_press index ${beg_press}

 # output options:
 # thermo_freq: output thermo snapshots at specified *time* interval
```

```
variable        thermo_freq index 10000
 # dump_freq: dump trajectory snapshots at specified *time* interval
variable        dump_freq index ${thermo_freq}
 # restart_freq: save restart file every N steps (0 = only at end, <0 = never)
variable        restart_freq index 1000000

# ___end command line variable section___

log ${outname}.lammpslog

# set up simulation
processors * * *
read_restart    ${infile}
neighbor        2.0 bin
neigh_modify    delay 5 check yes

kspace_style pppm 0.0001
#kspace_modify diff ad  # for large systems and many cores

variable        timestep index 1
timestep        ${timestep}
run_style       verlet

# change this to hold some atoms rigid
#group MOBILE union all
region MOBILE block INF INF INF INF 0 1 side out units box
group MOBILE region MOBILE
```

```
group FIXED subtract all MOBILE
neigh_modify exclude group FIXED FIXED
delete_bonds FIXED multi remove

# pick desired ensemble/integrator
# damping terms are in multiples of ${timestep}
variable _tdamp equal 100*${timestep}
variable _pdamp equal 1000*${timestep}
## NVE
  #fix NVE MOBILE nve
  #compute TFIX_temp MOBILE temp
## NVT
  #fix TFIX MOBILE nvt temp ${beg_temp} ${end_temp} ${_tdamp}
# NPT
  fix TFIX MOBILE npt temp ${beg_temp} ${end_temp} ${_tdamp} aniso ${beg_press} ${end_pr

# set up thermo data output
# kludge to get cumulative time
variable Time equal ${timestep}*step
# NVE
  thermo_style custom step v_Time temp epair emol etotal press vol
# NVT et al
  thermo_style custom step v_Time temp epair emol etotal press vol f_TFIX

# modify thermo data output
variable _thermo_freq equal ${thermo_freq}/${timestep}
thermo ${_thermo_freq}
```

```
thermo_modify flush yes
thermo_modify temp TFIX_temp

# set up dump/trajectory output -- potentially huge file!
variable _dump_freq equal ${dump_freq}/${timestep}
dump DUMP all custom ${_dump_freq} ${outname}.lammpstrj id type mol mass q xu yu zu vx v
dump_modify DUMP flush yes

# output useful info
variable Mass equal mass(all)
print "#@ mass := ${Mass}"
variable Charge equal charge(all)
print "#@ charge := ${Charge}"

# run simulation
if "${restart_freq} > 0" then "restart ${restart_freq} ${outname}.restart.*"
variable restart_freq_toggle equal ${restart_freq}/100
if "${restart_freq_toggle} > 0" then "restart ${restart_freq_toggle} ${outname}.restart.
run             ${numsteps}
if "${restart_freq} >= 0" then "write_restart ${outname}.restart.*"
```

Acknowledgement

This material is based upon work supported as part of the Center for Frontiers of Subsurface Energy Security, an Energy Frontier Research Center funded by the U.S. Department of Energy, Office of Science, Office of Basic Energy Sciences under Award Number DE-SC0001114.

Sandia National Laboratories is a multi-program laboratory managed and operated by Sandia Corporation, a wholly owned subsidiary of Lockheed Martin Corporation, for the U.S. Department of Energy's National Nuclear Security Administration under contract DE-AC04-94AL85000.

References

(1) Catti, M.; Ferraris, G.; Hull, S.; Pavese, A. Powder neutron diffraction study of 2M 1 muscovite at room pressure and at 2 GPa. *European Journal of Mineralogy* **1994**, *6*, 171–178.

(2) Cygan, R. T.; Liang, J. J.; Kalinichev, A. G. Molecular Models of Hydroxide, Oxyhydroxide, and Clay Phases and the Development of a General Force Field. *J. Phys. Chem. B* **2004**, *108*, 1255–1266.

(3) Cygan, R. T.; Greathouse, J. A.; Heinz, H.; Kalinichev, A. G. Molecular Models and Simulations of Layered Materials. *J. Mater. Chem.* **2009**, *19*, 2470–2481.

(4) Thyveetil, M.-A.; Coveney, P. V.; Greenwell, H. C.; Suter, J. L. Computer Simulation Study of the Structural Stability and Materials Properties of DNA-Intercalated Layered Double Hydroxides. *J. Am. Chem. Soc.* **2008**, *130*, 4742–4756.

(5) Wang, J. W.; Kalinichev, A. G.; Kirkpatrick, R. J.; Cygan, R. T. Structure, Energetics, and Dynamics of Water Adsorbed on the Muscovite (001) Surface: A Molecular Dynamics Simulation. *J. Phys. Chem. B* **2005**, *109*, 15893–15905.

(6) Greathouse, J. A.; Cygan, R. T. Molecular Dynamics Simulation of Uranyl(VI) Adsorption Equilibria onto an External Montmorillonite Surface. *Phys. Chem. Chem. Phys.* **2005**, *7*, 3580–3586.

(7) Berendsen, H.; Postma, J.; Van Gunsteren, W.; Hermans, J. Interaction Models for Water in Relation to Protein Hydration. *Intermolecular forces* **1981**, *11*, 331–342.

(8) Teleman, O.; Jonsson, B.; Engstrom, S. A Molecular-Dynamics Simulation of a Water Model with Intramolecular Degrees of Freedom. *Mol. Phys.* **1987**, *60*, 193–203.

(9) Raabe, G.; Sadus, R. J. Molecular Dynamics Simulation of the Dielectric Constant of Water: the Effect of Bond Flexibility. *J. Chem. Phys.* **2011**, *134*, 6.

(10) Raabe, G.; Sadus, R. J. Molecular Dynamics Simulation of the Effect of Bond Flexibility on the Transport Properties of Water. *J. Chem. Phys.* **2012**, *137*, 8.

(11) Wallqvist, A.; Teleman, O. Properties of Flexible Water Models. *Mol. Phys.* **1991**, *74*, 515–533.

(12) Smith, D. E.; Haymet, A. D. J. Simulations of Aqueous-Solutions - the Role of Flexibility and the Treatment of Long-Range Forces. *Fluid Phase Equilib.* **1993**, *88*, 79–87.

(13) Koneshan, S.; Rasaiah, J. C.; Lynden-Bell, R. M.; Lee, S. H. Solvent Structure, Dynamics, and Ion Mobility in Aqueous Solutions at 25 Degrees C. *J. Phys. Chem. B* **1998**, *102*, 4193–4204.

(14) Smith, D. E.; Dang, L. X. Computer-Simulations of Nacl Association in Polarizable Water. *J. Chem. Phys.* **1994**, *100*, 3757–3766.

(15) Cygan, R. T.; Romanov, V. N.; Myshakin, E. M. Molecular Simulation of Carbon Dioxide Capture by Montmorillonite Using an Accurate and Flexible Force Field. *J. Phys. Chem. C* **2012**, *116*, 13079–13091.

(16) Zhu, A.; Zhang, X.; Liu, Q.; Zhang, Q. A Fully Flexible Potential Model for Carbon Dioxide. *Chin. J. Chem. Eng.* **2009**, *17*, 268–272.

(17) Harris, J. G.; Yung, K. H. Carbon Dioxides Liquid-Vapor Coexistence Curve and Critical Properties As Predicted by a Simple Molecular-Model. *J. Phys. Chem.* **1995**, *99*, 12021–12024.

(18) Plimpton, S. J. Fast Parallel Algorithms for Short-Range Molecular Dynamics. *J. Comput. Phys.* **1995**, *117*, 1–19.

(19) Plimpton, S. J. LAMMPS Molecular Dynamics Simulator. `http://lammps.sandia.gov`.

(20) MartÃnez, L.; Andrade, R.; Birgin, E. G.; MartÃnez, J. M. PACKMOL: A Package for Building Initial Configurations for Molecular Dynamics Simulations. *J. Comput. Chem.* **2009**, *30*, 2157–2164.